Membrane permeability differentiation at the lipid divide

Urszula Łapińska[1], Georgina Glover[1], Zehra Kahveci[1,$], Nicholas A. T. Irwin[2,3], David S. Milner[3], Maxime Tourte[4], Sonja-Verena Albers[4], Alyson E. Santoro[5], Thomas A. Richards[3*], Stefano Pagliara[1*].

[1]Living Systems Institute and Biosciences, University of Exeter, Stocker Road, Exeter EX4 4QD, UK.
[2]Merton College, University of Oxford, Oxford OX1 4JD, UK
[3]Department of Zoology, University of Oxford, 11a Mansfield Road, Oxford OX1 3SZ, UK
[4]Molecular Biology of Archaea, Institute of Biology II, University of Freiburg, Schänzlestrasse 1, 79104, Freiburg, Germany
[5]Department of Ecology, Evolution and Marine Biology, University of California, Santa Barbara, California 93106, USA
[$]Current Address: Instituto de Nanociencia y Materiales de Aragón, CSIC-Universidad de Zaragoza, C/Pedro Cerbuna 12, Zaragoza 50009, Spain.
*s.pagliara@exeter.ac.uk thomas.richards@biology.ox.ac.uk

ABSTRACT

One of the deepest branches in the tree of life separates the Archaea from the Bacteria. These prokaryotic groups have distinct cellular systems including fundamentally different phospholipid membrane bilayers. This dichotomy has been termed the lipid divide and possibly bestows different biophysical and biochemical characteristics on each cell type. Classic experiments suggest that bacterial membranes (formed from lipids extracted from *Escherichia coli* for example) show permeability to key metabolites comparable to archaeal membranes (formed from lipids extracted from *Halobacterium salinarum*), yet systematic analyses based on direct measurements of membrane permeability are absent. Here we develop a new approach for assessing the membrane permeability of ~10 μm unilamellar vesicles, consisting of an aqueous medium enclosed by a single lipid bilayer. Comparing the permeability of eighteen metabolites demonstrates that diether glycerol-1-phosphate lipids with methyl branches, often the most abundant membrane lipids of known archaea, are permeable to a wide range of compounds useful for core metabolic networks, including amino acids, sugars, and nucleobases. Permeability is significantly lower in diester glycerol-3-phosphate lipids without methyl branches, the common building block of bacterial membranes. To identify the membrane characteristics that determine permeability we use this experimental platform to test a variety of lipid forms bearing a diversity of intermediate characteristics. We found that increased membrane permeability is dependent on both the methyl branches present on the archaeal phospholipid tails and the ether bond between the tails and the head group. These permeability differences must have had profound effects on the cell physiology and proteome evolution of early prokaryotic forms. To explore this further, we compare the abundance and distribution of transmembrane transporter-encoding protein families present on genomes sampled from across the prokaryotic tree of life. Archaea have a reduced repertoire of transporter gene families, consistent with increased membrane permeation. These results demonstrate that the lipid divide demarcates a clear difference in permeability function with implications for understanding some of the earliest transitions in cell evolution.

INTRODUCTION

Membranes are the boundaries that define cells. At some stage in early evolution, a molecular system must have become encapsulated within a lipid membrane [1] with functions that allowed metabolites to permeate the membrane and provide substrates for the molecular system to function. How metabolites cross membranes is therefore a key factor for understanding early evolution. Several key steps later, the prokaryotes emerged, cellular forms which include the Bacteria (once called Eubacteria) and the Archaea (once called Archaebacteria) [2–6]. The placement of the root of the prokaryotes is debated [7–9], making it difficult to understand the biology of the last universal common ancestor (LUCA). However, the Archaea/Bacteria bifurcation, which could represent LUCA, marks multiple important differences in cell biology. The consequences of these differences are key to understanding how the Archaea and Bacteria emerged.

Bacteria and Archaea possess homologous ribosomal proteins [6] and ribosomal RNA components [2], yet, Bacteria and Archaea possess distinct cell walls [10], DNA replication machineries (e.g. [11]), chromatin structures [12], and phospholipid membrane chemistries [13]. This latter distinction, termed the lipid divide [14], is an important evolutionary factor. Archaeal and bacterial phospholipid bilayers are assembled via distinct biosynthetic pathways [7]. Most Bacteria possess membranes of fatty-acid chains bonded to a glycerol-3-phosphate (G3P) backbone via ester bonds [7,13,15]. In contrast, mesophilic archaeal membranes are predominantly constructed from diether lipids [16] with isoprenoid chains containing methyl branches bonded to a glycerol-1-phosphate (G1P) backbone via ether bonds [7,13,15] (known as archaeol). These lipids often represent the abundant lipid forms [16] but both Bacteria and Archaea are able to synthesize a large diversity of structurally distinct lipids often in response to different environments [17]. For example, Archaea can increase the abundance of bipolar lipids (also known as tetraether caldarchaeol) in response to high temperatures [18].

The main function of cell membranes is to generate a semi-permeable solute barrier that allows for the development of chemical and proton gradients that drive the biochemistry and energetics of life [19]. The core difference between the G3P diester lipids of Bacteria and G1P diether lipids with methyl branches of Archaea could have a profound effect on the primary function of the cell membrane. *In vitro* studies have identified important biological implications of the physico-chemical properties of phospholipid membranes by using liposomes [20–29]. Liposomes are approximately spherical synthetic lipid bilayer membranes with a typical diameter of 100 nm that enclose an internal aqueous phase. A previous study using liposomes suggested that key metabolites from the environment could permeate prebiotically plausible membranes in the absence of transport machinery such as transmembrane transporter proteins [30]. However, this foundational work did not contrast the permeability of core metabolites across archaeal and bacterial-type membranes, but rather used mixtures of simple prebiotically plausible lipids, such as fatty acids, fatty alcohols and monoglycerides. An additional study has shown that, in the absence of counter-ions, liposomes made of diether lipids extracted from archaea (e.g. from *Halobacterium salinarum*) display lower permeability to protons compared to liposomes made of lipids extracted from bacteria (e.g. from *Escherichia coli*) [16]. This feature was confirmed using independent approaches [28,31,32]; the variation in proton permeability being likely due to the difference in the ether versus ester head-tail bond [33]. This differential permeability constitutes an important trait for understanding the differences in energetic functions of the Archaea and Bacteria [19]. It was also shown that bacterial and diether archaeal lipid membranes display similar permeabilities to glycerol, urea and ammonia [16]. However, these permeability traits were measured at high extracellular metabolite concentration (i.e. 200 mM) using indirect spectroscopic techniques, which average over a large number of

liposomes and associated impurities (e.g. multi-lamellar liposomes and lipid aggregates). As such there are a number of potential limitations of these results: i) they are based on ensemble measurements across variant lipid architectural forms, ii) they do not investigate permeability characteristics of cellular metabolites at biologically/ecologically realistic substrate concentrations, and iii) they investigate a limited number of metabolites. Collectively, this means that there is a limited understanding of the implications of membrane chemistry variation on metabolite permeability in biologically relevant contexts, particularly given recent evidence suggesting that living cells can obtain nutrients from the environment in a transporter protein-independent fashion [34].

Here we test the hypothesis that core archaeal and bacterial type lipid membranes have fundamentally different permeability traits directly implying that the ancient Archaea/Bacteria bifurcation would also encompass a distinct change in metabolite permeability. Such a difference would have profound effects for the evolution of membrane transporter repertoires, intracellular metabolic networks, and associated cellular ecologies. We present a new approach for the study of membrane permeability based on microfluidic manipulation of unilamellar vesicles composed of a single phospholipid bilayer of archaeal or bacterial membrane mimics. Our results show that the lipid divide demarcates a dichotomy in membrane permeability characteristics. In contrast to previous ideas, membranes composed of archaeal core phospholipids display elevated permeability to many compounds key for core metabolic functions. Using phylogenomic approaches, we also demonstrate that this functional difference correlates with variations in the evolution of the transporter protein encoding gene repertoire.

RESULTS AND DISCUSSION

Microfluidic screening to explore membrane permeability characteristics

Here we report a system to enable the capture and individual placement of unilamellar vesicles obtained via electroformation of synthetic lipids (see Methods) in multiple parallel arrays of tens of vesicles using microfluidics (Figure 1). This approach enabled us to precisely control the chemostatic fluid environment of the vesicles [35]. The diameter of these vesicles is in the range of 5- to 15-μm. Although such diameter range is large for prokaryotic cell sizes, these dimensions were chosen to aid imaging and manipulation. In order to measure metabolite permeation into the unilamellar vesicles, we loaded the vesicles with a neutral pH buffer and carboxyfluorescein (CF), a fluorescent dye which allows direct assessment of molecular uptake by variations in fluorescent properties in response to changes in intra-vesicle metabolite concentration [16,36]. In fact, the introduction of metabolites in the vesicle reduces the self-quenching properties of carboxyfluorescein, resulting in increased vesicle fluorescence. Therefore, a relative increase in intra-vesicle fluorescence indicates membrane permeability to the target metabolite when delivered via continuous flow through the microfluidic device (Figure 1 and Methods). Individual metabolites were delivered into the extra-vesicle environment (also containing a neutral pH buffer), while imaging the changes in fluorescence levels of multiple individually trapped vesicles (Figure 1 and Methods). By using this experimental approach, we conducted parallel controlled experiments exploring how cellular metabolites can cross membranes of different phospholipid chemical composition using changes in CF fluorescence as a reporter for membrane permeability to metabolites.

We first studied the permeability of single vesicles composed of synthetic lipids with isoprenoid chains containing methyl branches bonded to a glycerol-1-phosphate (G1P) backbone via ether bonds (archaeal-like membrane phospholipids – abbreviated here as ‘archaeal 4ME diether G1PC’) (lipid 1 in Table S1) or synthetic

lipids with fatty acids bonded to a glycerol-3-phosphate (G3P) backbone via ester bonds (bacterial-like membrane phospholipids – ternary lipid mixture abbreviated here as 'bacterial diester G3PE-PG-CA', lipid 2 in Tables S1) to eighteen small metabolites (Table S2). Notably, synthetic G1P diether lipids with methyl branches are not commercially available, to our knowledge, and were therefore synthesised *de novo* for the purpose of this study (see Methods). We chose metabolites with different molecular weight, hydrophobicity, and number of rotatable bonds (see Table S2).

Our single-vesicle measurements revealed heterogeneity in the permeability of each synthetic lipid type to each metabolite, with some vesicles of each lipid type displaying a decrease in intracellular fluorescence during the delivery of each metabolite while other vesicles displayed an increase in intracellular fluorescence (temporal dependence of single-vesicle fluorescence for archaeal 4ME diether G1PC lipids and bacterial diester G3PE-PG-CA lipids are reported with dashed magenta lines and dashed-dotted blue lines in Figure S1). For example, the coefficient of variations in the permeability of archaeal 4ME diether G1PC vesicles and of bacterial diester G3PE-PG-CA vesicles to aspartic acid, glyceraldehyde and adenine, were 118% and 103%, 60% and 198%, 76% and 108% (Figure S1D, S1G and S1Q, respectively), in accordance with the proposition that lipid membranes are a system with heterogeneous functions [37,39–43].

Therefore, in order to compare the permeability of different synthetic lipid types to the same metabolite, we carried out Mann-Whitney two-tailed statistical comparisons between the distributions of intra-vesicle fluorescence after 3 minutes of delivery of each metabolite for each synthetic lipid type. Temporal dependence of fluorescence distribution means and standard deviations are reported in Figure 2 (magenta triangles and dashed lines for archaeal 4ME diether G1PC vesicles, blue squares and dashed-dotted lines for bacterial diester G3PE-PG-CA vesicles) together with single-vesicle fluorescence distributions and Mann-Whitney two-tailed statistical comparisons at t=3 (further details about Mann-Whitney two-tailed statistical comparisons are reported in Supplementary file 1).

We found that archaeal 4ME diether G1PC vesicles were significantly more permeable to the amino acids glycine, alanine, leucine, aspartic acid, tryptophan and glutamine compared to bacterial diester G3PE-PG-CA vesicles (Figure 2A-2F, Figure S1A-S1F, Supplementary file 1). Consistent with the amino acid findings, archaeal 4ME diether G1PC vesicles were also more permeable to the sugar's glyceraldehyde, glycerol, deoxyribose, ribose and arabinose compared to bacterial diester G3PE-PG-CA vesicles (Figure 2G-2K, Figure S1G-S1K, Supplementary file 1), whereas we did not measure a significant difference in the permeability to dihydroxyacetone (Figure 2L, Figure S1L, and Supplementary file 1). Interestingly, the difference in permeability was strongly distinct for three large sugar types, deoxyribose, ribose, and arabinose, the two former sugars including primary constituents of the hereditary materials DNA and RNA, respectively.

Finally, archaeal 4ME diether G1PC vesicles were also more permeable to the amide urea, and the nucleobases cytosine, uracil, guanine and adenine compared to bacterial diester G3PE-PG-CA vesicles (Figure 2M-2Q, Figure S1M-S1Q, Supplementary file 1). These data suggest that important nitrogen sources and components of DNA and RNA can permeate archaeal 4ME diether G1PC vesicles. The phosphonate 2-aminoethyl phosphonic acid (Figure 2R, Figure S1R, Supplementary file 1) showed no significant difference in permeability characteristics between the two types of vesicles. We also attempted to measure permeabilities to the nucleotide adenosine monophosphate, however, during pilot studies the vesicles burst during delivery of this chemical and so we did not test this substrate further.

Pooling together the data for the eighteen metabolites investigated, we did not find a significant correlation between permeability and lipid molecular weight or hydrophobicity (Pearson coefficient r = -0.22,

0.36, respectively, for archaeal 4ME diether G1PC vesicles; r = 0.09, 0.24, respectively, for bacterial diester G3PE-PG-CA vesicles; none significant at p = 0.05; Table S2). These data suggest that the metabolic selectivity of these membrane mimics is complex and does not rely solely on basic molecular properties such as molecular weight or hydrophobicity. Taken together with previous findings demonstrating that solute hydrophobicity correlates poorly with permeability coefficients of eukaryotic fatty acid or phospholipid membranes [36], our data corroborate the hypothesis that subtle variations in the metabolite atomic structure could contribute to differences in membrane permeability [36–38]. In fact, we found a significant correlation between permeability and rotatable bond number for archaeal 4ME diether G1PC vesicles (Pearson coefficient r = -0.49, *) but not for bacterial diester G3PE-PG-CA vesicles (r = -0.32, non-significant at p = 0.05).

The striking difference in CF fluorescence between archaeal 4ME diether G1PC and bacterial diester G3PE-PG-CA vesicles was confirmed when we extended the duration of our permeability experiments from 3 to 6 minutes (Figure S2). Moreover, the dimensions of each vesicle did not significantly change during metabolite delivery (Figure S3), confirming that vesicle deformation did not occur in our experiments and did not play a role in the observed differences in permeability traits between archaeal 4ME diether G1PC vesicles and bacterial diester G3PE-PG-CA vesicles. Such differences were also not attributable to differential metabolite accumulation within the lipid bilayers, since: i) CF has very low affinity for the lipid hydrophobic chains [16], so interactions with substrates within the membrane are unlikely; ii) CF fluorescence intensity was uniform across whole vesicles for both lipid type and the full range of metabolites investigated, consistent with previous data obtained on fatty acid and phospholipid liposomes [16,36]. Our data do not allow us to infer a detailed kinetics of the permeation of each metabolite and could be complemented via pulse-chase experiments requiring faster fluidic exchanges. Therefore, we did not attempt to extract absolute kinetic parameters, such as the permeability coefficient, but centred this current work on directly comparing changes in CF fluorescence (as a proxy for permeability) between archaeal 4ME diether G1PC and bacterial diester G3PE-PG-CA vesicles. However, we were able to observe differences in terms of both the uptake onset and slope for different metabolites. For example, glycine, ribose and uracil displayed a steep uptake during the first minute of their delivery to archaeal 4ME diether G1PC vesicles (Figure 2A, 2J and 2O, respectively), whereas the uptake of aspartic acid, glutamine and dihydroxyacetone started only after the first minute of their delivery to archaeal 4ME diether G1PC vesicles (Figure 2D, 2F and 2L). These data demonstrate that metabolites are not passing across vesicles via puncture holes generated during vesicle formation but by genuine diffusion through the lipid bilayers in a metabolite-specific manner.

As discussed in the introduction, natural archaeal membranes are formed from heterogenous mixtures of lipids some with tetraether bipolar lipids (e.g. caldarchaeol) which act to directly connect the membrane bilayers, a function that is likely to increase the stiffness of the membrane and reduce permeability [44]. Such mixtures might have different properties than the homogenous membranes studied here. To explore this possibility, we attempted to use lipids extracted from *Haloferax volcanii*, predominantly containing diether lipids with head group derivatives of phosphatidylglycerol [45], and lipids extracted from *Sulfolobus acidocaldarius*, predominantly containing tetraether lipids with head group derivatives of phosphatidylhexose [46]. However, we could not obtain mechanically stable vesicles via electroformation for either of these lipid mixtures. It is therefore important to mention that our experiments do not reveal the permeability traits of extant prokaryotic membrane mixtures but rather identify the contrasting permeability traits of the common and core building blocks of the archaeal and bacterial membranes.

Finally, we wanted to rule out that the relatively lower permeability of bacterial diester G3PE-PG-CA vesicles could be due to interactions between different lipids within the ternary lipid mixture that we employed to mimic more closely bacterial membranes (lipid 2 in Table S1). To do so, we measured and contrasted permeability to urea, glycine, ribose, deoxyribose, glycerol and phosphonate in vesicles made of bacterial ternary-lipid mixtures (G3PE-PG-CA, lipid 2 in Table S1) and vesicles made of single lipids (G3PE, lipid 6 in Table S1) and found that these two different bacterial mimics displayed comparably low permeabilities to all the metabolites tested (Figure S4).

Which archaeal lipid characteristics determine permeability traits?

To uncover the chemical determinants of archaeal membrane permeability, we employed vesicles made of a range of lipids with a mixture of archaeal and bacterial lipid characteristics. We tested the impact of the lipid chain branching, length, tail-head bond (ester/ether) and the G1P vs G3P backbone on membrane permeability. We performed these experimental tests using urea, glycine, ribose, deoxyribose, glycerol and phosphonate towards which archaeal 4ME diether G1PC vesicles and bacterial diester G3PE-PG-CA vesicles display different patterns of permeabilities (Figure 2).

Firstly, we electroformed vesicles by using a lipid that carried a bacterial-like glycerol-3-phosphate (G3P) backbone but with archaeal like diether tail-head bond and isoprenoid chains containing methyl branches (4ME diether G3PC, lipid 3 in Table S1, green circles in Figure 3). The permeabilities of these hybrid vesicles to the six metabolites investigated were not significantly different to the permeabilities of archaeal vesicles (4ME diether G1PC, lipid 1 in Table S1, magenta upward triangles in Figure 3 and Supplementary file 1) but were significantly higher than the permeabilities measured for the bacterial vesicles (diester G3PE-PG-CA, lipid 2 in Table S1, blue squares in Figure 3, Kruskal-Wallis one-way analysis of variance statistical comparisons are reported in Supplementary file 2). These data suggested that the change from a G1P to a G3P backbone was not a key factor in determining membrane permeability.

Next, we tested a different hybrid lipid with the bacterial-like glycerol-3-phosphate (G3P) backbone but with archaeal-like diether tail-head bond and isoprenoid chains without methyl branches (Diether G3PC, lipid 4 in Table S1 and black diamonds in Figure 3). We found that in the absence of lipid chain branching, these hybrid vesicles displayed a statistically significant and consistently lower permeability compared to archaeal 4ME diether G1PC vesicles (magenta upward triangles in Figure 3 and Supplementary file 2). This striking difference is possibly due to increased membrane fluidity in the presence of methyl branched lipid chains [30,47]. In the absence of methyl branching, these hybrid diether G3PC vesicles displayed permeabilities to urea, glycine, deoxyribose or ribose that were comparable to the permeabilities measured for bacterial diester G3PE-PG-CA vesicles (lipid 2 in Table S1 and blue squares in Figure 3A, 3B, 3E and 3F, respectively, none significantly different at $p = 0.05$, Supplementary file 2). In contrast, permeabilities to glycerol and phosphonate were lower in the hybrid diether G3PC vesicles without methyl branching compared to bacterial diester G3PE-PG-CA vesicles (Figure 3C and D, * and *, respectively, Supplementary file 2).

A third hybrid lipid with the bacterial-like glycerol-3-phosphate (G3P) backbone and a diester tail-head bond but with archaeal-like isoprenoid chains with the methyl branches was also compared in a similar manner (4ME Diester G3PC, lipid 5 in Table S1, brown downward triangles in Figure 3). In the absence of an ether bond (substituted with an ester bond), 4ME diester G3PC vesicles displayed significantly lower permeabilities to all six metabolites investigated compared to archaeal 4ME diether G1PC vesicles (magenta upward triangles in Figure 3 and Supplementary file 2), and exhibited permeabilities similar to bacterial diester G3PE-PG-CA

vesicles (blue squares in Figure 3, none significantly different apart from permeability to ribose that was significantly lower in 4ME Diester G3PC vesicles, *, Supplementary file 2). Taken together these data demonstrate that increased membrane permeability can be achieved via the simultaneous use of an ether bond and methyl chain branching, both of which characterize the core lipids of archaea.

To follow on from this, we set out to determine whether permeability is affected by variations in the archaeal lipid head (lipid 7 in Table S1). However, despite attempting different electroformation protocols (see Table S4) we could not produce vesicles using this lipid, possibly because this lipid forms non-lamellar structures of either a cubic or hexagonal fashion [48]. We note, however, that previous studies suggest that lipid headgroup composition has only limited impact on the permeation of small molecules [29].

Next, we investigated how permeability varies in phospholipids according to chain length. Synthetic G1P lipids with methyl branches are not commercially available, so we focused on the study of G3P lipids without methyl branches and with variant chain lengths (lipids 4, 8, 9 in Table S1). These experiments provide no evidence for a significant correlation between lipid chain length (C=12, C=16 and C=18, i.e. lipids 8, 4 and 9 in Table S1) and permeability to any of the metabolites investigated (Figure S5, Pearson correlation coefficient r=-0.58, 0.95, 0.52, -0.10, -0.69 and 0.30 for urea, glycine, glycerol, phosphonate, deoxyribose and ribose, respectively), corroborating previous findings on eukaryotic membrane mimics [49]. Significant differences in permeability to water and weak acids were previously observed only for large variations in chain length; an increase from 14 to 26 in the length of acyl chains of eukaryotic lipids led to a five-fold decrease in permeability [29]. Accordingly, our data show that a short chain length slightly favoured permeability to urea and deoxyribose (Figure S5A and S5E, respectively). In contrast, a long chain length slightly favoured permeability to glycine and ribose (Figure S5B and S5F, respectively), but overall, these effects were masked by vesicle-to-vesicle variation in permeability to these metabolites. Furthermore, we attempted to produce vesicles using lipids of other chain lengths (C=6 and C=14, i.e. lipids 10 and 11 in Table S1). However, these vesicles appeared to be mechanically unstable, possibly because their transition temperature is close to the temperature at which we carried out our membrane permeability assays. We note, these comparisons did not include variations in the number of methyl branches per chain so our experiments do not rule out the possibility that differences in the number of methyl branches may alter permeability characteristics.

Our next experiments demonstrated that decreasing bonding saturation (i.e. single bonds that were more likely present in prebiotic molecules [30] versus double bonds) along hybrid G3P diether phospholipids of fixed chain length (C=18, lipid 12 in Table S1) significantly decreased permeability to the small amide, urea, and, to a lesser extent, to the small amino acid, glycine, compared to bonding unsaturation (i.e. double bonds, lipid 11 in Table S1, Figure S6A and S6B, *** and *, respectively). However, bonding saturation did not have an impact on the permeability to glycerol, phosphonate, deoxyribose, or ribose (Figure S6C, S6D, S6E and S6F, respectively, none significantly different), whereas previous studies using G3P diester phospholipids or fatty acid liposomes found increased permeability to glycerol [29] and ribose [30] liposomes made of unsaturated lipids.

Tetraether bonds, generating bipolar lipids (or caldarchaeol), or cyclopentane rings along the caldarchaeol chains could further affect the permeability traits in archaeal membrane mimics. Given the variance of these lipid forms across Archaea [50] and the observation that such variants are the minority constituents in some archaeal membranes [51,52], we suggest they are of lesser importance for understanding the evolution of core/ancestral permeability functions in ancestral cell forms carrying archaeal lipids. However, we do acknowledge that introduction of these lipid variations is likely to alter permeability [53] and is an

important factor for determining the ecology of extant Archaea. The experimental platform presented is readily adaptable to investigate the effect of further chemistry variations, however, these synthetic lipids are not currently commercially available. Future work should explore the effect of lipid mixtures on permeability traits. Furthermore, we did not investigate the effect on permeability of membrane variants embedding an S-layer, a peptidoglycan layer, or an outer membrane such as those seen in diderm bacteria, because all these features are predicted to follow the archaeal/bacterial bifurcation and so represent secondary elaborations relative to the lipid divide. We also acknowledge that permeability traits can vary with changes in environmental conditions such as pH (which we kept constant at 7.4), temperature (which we kept constant at 22 °C) or salinity levels [54,55] and the differences we have observed are likely subject to variation in different environmental conditions. Although our experimental platform could be adapted to investigate permeability traits under variant environmental conditions, there are constraints as vesicles suffer damage in the presence of low or high pH and/or salinity. Moreover, lipids change state above or below the transition temperature. Therefore, the experimental platform would need further development to physically stabilise vesicles, by using, for example, higher density media or by forming vesicles on physical support structures. However, such experiments would tell us much about the conditions in which cellular chasses evolved.

Membrane permeability negatively correlates with transporter gene repertoires

The observed differences in membrane permeability imply that any transition between archaeal and bacterial-type membrane chemistries would require extensive recalibration of numerous cellular systems in response to changes in permeability, osmotic stress, and metabolite homeostasis. Such a transition could be facilitated by a mixed archaeal-bacterial membrane [7,56], but the ultimate change would require adaptation to these altered cellular properties. The evolution of membrane transporters could permit a reduction in lipid membrane permeability, for example, if a cell was to transition from an archaeal-like membrane to a bacterial-like membrane, as predicted under some hypotheses for the origins of the eukaryotes [57,58]. Accordingly, given the increased permeability of the core archaeal lipid membranes shown here, we hypothesized that archaeal genomes would encode a significantly reduced complement of transporter gene families relative to Bacteria, particularly for those protein families known to transport metabolites capable of permeating archaeal lipid membranes (shown in Figure 2). A limited transporter repertoire could reflect a reduced dependency on protein-based translocation systems as metabolite requirements could be satisfied by a combination of core metabolic function and lipid membrane permeability. Likewise, increased membrane permeability may limit the utility of membrane transporters by decreasing transport efficiency or impairing the formation of concentration gradients.

To test this hypothesis, we iteratively searched diverse bacterial (n = 3,044) and archaeal (n = 243) genome-derived predicted proteomes using profile hidden Markov models (HMM, n = 277) derived from TCDB (Transporter Classification Database) protein families [59], to identify previously classified transporter homologs across prokaryotes. Despite the sensitivity of our search, the Archaea had fewer transporters relative to the Bacteria, irrespective of bacterial membrane system (e.g., monoderms or diderms) and regardless of whether transporter numbers were normalised to the total number of proteins per genome (Figure 4A and Figure S7A). Certain transporter families were consistently encoded across prokaryotes, including many ion transporters (see cluster 2 in Figure 4A, largely composed of ion transporters), which are required due to the impermeability of both membrane types to ions, with the exception of protons [49]. In contrast, other families showed significantly reduced representation in Archaea (see clusters 1, 3, and 5 in Figure 4A which

were functionally heterogeneous, whereas cluster 4 comprised outer membrane transporters associated with diderms). In particular, transporter families known to translocate metabolites similar to those that permeate archaeal membrane mimics (e.g., amino acids, sugars and nucleobases shown Figure 2) were significantly depleted even when accounting for differential taxon sampling bias using bootstrap resampling (Figure 4B).

It has previously been argued that protein-membrane interactions, attuned to the specific lipid characteristics of either bacterial or archaeal membranes, may have acted to enforce the lipid divide as the Bacteria and Archaea diversified [14]. Therefore, to account for the possibility that archaeal transporters were not accurately recovered in our searches due to divergent biochemical characteristics or a lack of archaeal transporter family representation in TCDB, we first examined the possibility that archaeal membrane transporters have transmembrane (TM) domains with different lengths or alternative amino acid compositions, a factor that may have obscured previous HMM based annotations of transporter gene families. Comparisons between over 10.8 million bacterial and 528,000 archaeal TM domains (identified from over 2.2 million bacterial and 116,000 archaeal transporter proteins) revealed no significant differences in TM domain characteristics between Archaea and Bacteria (Figure S7B, S7C), suggesting that these biochemical properties would neither impair bioinformatic detection nor would limit horizontal gene transfer of transporter proteins from Bacteria to Archaea [14]. However, we note that differences may be obscured because of lower archaeal sampling and absence of systematic functional studies of archaeal transporters not identified by cross referencing bacterial transporter families.

Secondly, to identify putative archaeal transporters that may have been absent from the TCDB database, we clustered archaeal proteins into protein families and identified those with characteristics indicative of transporter proteins (a median of at least four TM domains and annotation with transporter-associated PFAM domain). This search revealed only thirteen previously unsampled putative transporter families (mostly branched-chain amino acid permeases, ABC- and EamA-transporters) that were predicted to function in metabolite uptake and were present in at least a quarter of archaeal species (Supplementary file 2). However, only a single undetected putative ABC-transporter family was identified in over 50% of archaeal species (70.8%). These results strongly indicate that unidentified transporters do not account for the reduced transporter repertoire observed in Archaea (Supplementary file 2). Together, these results are consistent with a reduced dependency on metabolite transporter proteins in Archaea, an evolutionary outcome which could reflect a reduced transporter repertoire in the last archaeal common ancestor or frequent transporter losses in individual archaeal lineages. Regardless, transporter reduction may have been facilitated, in part, by the increased metabolite permeability of archaeal lipid membranes which, in turn, reduces the requirement for, or utility of, transporter proteins.

CONCLUSIONS

The deepest branch in the tree of life separates the Archaea and the Bacteria. This ancient node demarks two different core membrane chemistries known as the lipid divide. There is considerable variation in membrane composition on both sides of the lipid divide, but fundamentally these membranes are built of two different phospholipid chemistries. Here we demonstrate that homogenous versions of the archaeal and bacterial core lipid membranes show distinct differences in permeability characteristics when generated using electroformation. Archaeal-type lipid membranes show permeability to a range of compounds that would theoretically be useful to known cellular metabolic networks. Our data demonstrate that archaeal membrane permeability is dependent on the simultaneous presence of methyl chain branching and ether bond properties,

two hallmarks of archaeal lipids. This selective permeability could have provided early cellular forms with access to specific metabolic resources, from which a metabolic network could arise and diversify. Taken together with previous findings demonstrating that archaeal lipid membranes display low permeability to ions [16], these data support the suggestion that early cellular forms without a dedicated protein based transmembrane transportation system would be more likely to acquire stable and diversified metabolic functions using an archaeal lipid membrane than a bacterial lipid membrane [7].

METHODS

Preparation of materials

All chemicals were purchased from Merck. All lipids [i.e. lipid 1 (1,2-di-O-phytanyl-sn-glycero-3-phosphocholine), lipid 2 (1,2-dioleoyl-sn-glycero-3-phosphoethanolamine, 1,2-dioleoyl-sn-glycero-3-phospho-(1'-rac-glycerol), 1,3-*bis* (*sn*-3'-phosphatidyl)-*sn*-glycerol), lipid 3 (1,2-dioleoyl-sn-glycero-3-phosphoethanolamine), lipid 4 (1,2-di-O-hexadecyl-*sn*-glycero-3-phosphocholine), lipid 5 (1,2-diphytanoyl-sn-glycero-3-phosphocholine), lipid 6 (1,2-di-O-phytanyl-sn-glycero-3-phosphoethanolamine), lipid 7 (1,2-di-O-dodecyl-sn-glycero-3-phosphocholine), lipid 8 (1,2-di-O-octadecyl-sn-glycero-3-phosphocholine), lipid 9 (1,2-di-O-hexyl-sn-glycero-3-phosphocholine), lipid 10 (1,2-di-O-tetradecyl-sn-glycero-3-phosphocholine) and lipid 11 (1,2-di-O- (9Z-octadecenyl)-sn-glycero-3-phosphocholine), see Table S1] were purchased from Avanti Polar Lipids within Merck. Indium tin oxide (ITO) coated glass slides were purchased from VisionTek Systems Ltd. The fluorescent probe 5(6)-carboxyfluorescein (CF), (MW=376 g/mol), was dissolved in absolute ethanol at a stock concentration of 10 mg/mL. In order to perform all permeability experiments at physiological pH (7.4), the washing buffer was prepared by dissolving sucrose (MW=342 g/mol) in 5 mM 4-(2-hydroxyethyl)-1-piperazineethanesulfonic acid (HEPES) at pH=7.4 at a final sucrose concentration of 195 mM. This washing buffer was used for three purposes: i) to dissolve all tested metabolites, ii) to electroform vesicles of all lipid chemistries, and iii) to wash away from the chip the extra-vesicle fluorescent probe CF. All tested metabolites [i.e. glycine (product number G7126 in Merck), alanine (A7627), leucine (L8000), aspartic acid (A9256), glutamine (G8540), tryptophan (T0254), glyceraldehyde (G5001), dihydroxyacetone (PHR1430), deoxyribose (31170), ribose (R7500), arabinose (A3256), glycerol (G9012), cytosine (C3506), uracil (U0750), adenine (A8626), guanine (G11950), urea (U5378), (2-aminoethyl)phosphonic acid (268674) and adenosine monophosphate (A1752), see Table S2], were dissolved in the washing buffer at a final concentration of 1 mM.

De novo synthesis of the archaeal 4ME diether G1PC lipid

1,2-di-O-phytanyl-sn-glycero-1-phosphocholine (i.e. 4ME diether G1PC, lipid 1 in Table S1) was not commercially available during this project and therefore was synthesized *de novo* by Avanti Polar Lipids based on a previously reported procedure [60] with slight modifications starting with commercially available (R)-Solketal. Enquiries about the synthesis and availability of this lipid should be directed to Avanti Polar Lipids.

Preparation of synthetic lipid vesicles

Giant unilamellar vesicles (simply referred as vesicles in the manuscript) were electroformed by using Vesicle Prep Pro (Nanion). The phospholipid of interest was weighed and dissolved in chloroform at a stock concentration of 10 mM. Next, 10 µL of each phospholipid solution was spread evenly using a pipette (Starlab) on the conductive side of an ITO-glass slide. The glass slide was then placed in a vacuum desiccator for 15 min to dry out the lipid solution. Meanwhile, the washing buffer was prepared as described above, and 495 µL of this buffer was degassed and mixed with 5 µL of CF stock solution (10 mg/mL) at a final CF concentration of 0.266 mM. The ITO-slide coated by a dry lipid layer was then placed inside the Vesicle Prep Pro chamber and a greased rubber O-ring was placed around the dry lipid layer. The area within the O-ring was then filled with 300 µL of 0.266 mM CF solution. A second ITO-slide was placed above the O-ring with its conductive side facing downwards and the Vesicle Prep Pro chamber was then closed. The electroformation process was carried out using a different electroformation protocol for each lipid or lipid mixture employed (see Table S3).

Briefly, the electroformation process was performed in three steps. The rise step: the AC voltage was linearly increased peak to peak (p–p) from 0 V till the maximum chosen value (see Table S3). The main step: the voltage was kept constant for the chosen duration (see Table S3). The fall step: the voltage was decreased linearly to 0 V. For lipids 9 and 10 none of the protocols employed yielded mechanically stable vesicles. For lipid 6 none of the employed protocols allowed vesicle electroformation possibly because this lipid forms non-lamellar structures of either a cubic or hexagonal fashion [48]. The protocols for the electroformation of vesicles made of lipids 7, 8 and 11 were adapted from [61]. The final fluorescent vesicle suspension consisted of fluorescent vesicles (because of the embedded CF molecules) and free CF molecules in the washing buffer. This suspension was collected from the ITO-slide surface using a pipette, placed in an Eppendorf microcentrifuge tube for storage at 4 °C and used within five days.

Extraction of natural lipids

Lipids were extracted from the halophilic *Haloferax volcanii* (100 % diether lipids; [45]) and from the thermoacidophilic *Sulfolobus acidocaldarius* (*ca.* 10 and 90 % diether and tetraether lipids, respectively [62]). *H. volcanii* DS2 was grown at 45 °C, pH 7.2 in Hv-CAB medium containing per liter: 145.0 g NaCl, 17.5 g $MgCl_2 \cdot 6H_2O$, 20.5 g $MgSO_4 \cdot 7H_2O$, 4.1 g KCl, 300.0 mg $CaCl_2 \cdot 2H_2O$, 23.0 mg $FeSO_4 \cdot 7H_2O$, 4.4 mg $ZnSO_4$ $7H_2O$, 3.6 mg $MnCl_2 \cdot 4H_2O$, 0.5 mg $CuSO_4 \cdot 7H_2O$, 1.4 g Tris-HCl, 5.0 g casamino acids, 50.0 mg uracil, 1.0 mg thiamine and 1.0 mg biotin. *S. acidocaldarius* DSM639 was grown at 75 °C, pH 3.0 in Brock medium containing per liter: 1.3 g $(NH_4)_2SO_4$, 280.0 mg KH_2PO_4, 250.0 mg $MgSO_4 \cdot 7H_2O$, 70.0 mg $CaCl_2 \cdot 2H_2O$, 20.0 mg $FeCl_3 \cdot 6H_2O$, 4.5 mg $Na_2B_4O_7 \cdot 10H_2O$, 1.8 mg $MnCl_2 \cdot 4H_2O$, 220.0 µg $ZnSO_4 \cdot 7H_2O$, 50 µg $CuCl_2 \cdot 2H_2O$, 30 µg $Na_2MoO_4 \cdot 2H_2O$, 20 µg $VOSO_4 \cdot 2H_2O$, 5 µg $CoSO_4 \cdot 7H_2O$, 1.0 g NZ-amine and 2.0 g dextrin. Both species were grown with stirring (150 rpm), air bubbling (5 l min^{-1}) and 10.0 ml of antifoam 204 (Sigma-Aldrich; Sain-Louis, MO, USA). Cells in late exponential phase were centrifuged (4000 × g, 4 °C, 20 min), flash-frozen in $N_{2, liq}$ and freeze-dried overnight. 2.0 g of dried biomass were extracted for 8 h in a soxhlet extractor containing 400 ml of a 1:9 (*v*/*v*) mixture of methanol (MeOH) and dichloromethane (DCM). The resulting total lipid extract was dried under reduced pressure, resuspended in 250 ml of H_2O/MeOH (1:1, *v*/*v;* F1) and applied onto a Sep-Pak® Vac 20 cc C18 cartridge (Waters; Milford, MA, USA). The column was then eluted with 250 ml of H_2O/MeOH/DCM (1:2.5:1, *v*/*v*/*v*; F2), 100 ml of H_2O/MeOH/DCM (4:25:65, *v*/*v*/*v*; F3) and 100 ml of MeOH/DCM (1:9, *v*/*v*; F4). F3 was again dried under reduced pressure, weighted and stored at -20 °C until further use. We made several different attempts to electroform vesicles using these extracted lipids and the electroformation steps. We employed five different rise steps with a peak to peak amplitude of 1, 1.6, 3, 5.3, or 10 V; four different durations for the main step 90, 120, 160 or 360 min. We also explored three different AC frequencies 5, 10, or 500 Hz and four different temperature values 37, 40, 45, or 65 °C.

Design and fabrication of the microfluidic chip

The microfluidic chip was designed in AutoCAD and consisted of two inlets connected to a main chamber which splits into four parallel channels, containing 60 hydrodynamic traps each (henceforth coves) and further connected to a single outlet with an overall footprint of 0.8 mm × 1.3 mm (Figure 1). Each cove was designed by drawing two concentric circles of radii 15 and 35 µm, respectively. A straight vertical line was drawn on the diameter of the outer circle from top to bottom and the left sides of the two semi-circles were deleted. A second 10 µm long vertical line was drawn within the inner semi-circle, followed by two horizontal semi-infinite lines starting at the vertices of this line. The whole area included in these three lines was then deleted, yielding the

final design of each cove. In first approximation, this shape resembles a cove with an opening in the middle. This design was printed on a film mask (Microlithography Services Ltd) and used for fabricating a mold of the fluidic chip via photolithography [63,64]. Briefly, a 20 µm thick layer of SU-8 3025 (Microchem) was deposited via spin coating (6,000 r.p.m. for 30 s) on a silicon wafer (Si-Mat Silicon Materials), baked at 95 °C for 10 min, exposed to ultraviolet light (1.3 s, 400 nm, 50 $mWcm^{-2}$) through the film mask above and developed after baking at 65 °C for 2 min and 95 °C for 3 min. Polydimethylsiloxane (PDMS) replica of this device were produced via soft lithography as previously described [65,66]. Briefly, a 10:1 (base:curing agent) PDMS mixture (SYLGARD™ 184 Silicone Elastomer Kit, Dow) was cast on the mold, degassed for 30 min and cured at 70 °C for 2h in an oven. The cured PDMS was peeled from the mold and fluidic accesses were created by using a 1.5 mm biopsy punch (Integra Miltex). Oxygen plasma treatment was used to irreversibly seal the PDMS chip on a glass coverslip (10 s exposure to 30 W plasma power, Plasma etcher, Diener Electronic GmbH). We note that, compared to microfluidic devices previously employed for single-cell confinement [67,68], our approach relies on a single height device that can be fabricated in a single step without the use of dedicated photolithography equipment and can be easily carried out by users who might not be familiar with the technical aspects of microfabrication.

Microfluidic permeability assay

15 µL of washing buffer was injected in the microfluidic chip from the buffer inlet (Figure 1) using a pipette until the buffer spilled out from both the metabolite inlet and the outlet. Next, the metabolite inlet was temporarily sealed with a 1 cm × 1 cm piece of Scotch Magic™ tape and 15 µL of the fluorescence vesicle suspension was pipetted into the chip via the washing buffer inlet. Once a cove had been occupied by a vesicle, the amount of fluid entering the cove was reduced [67] but still allowed molecular diffusion in the cove, which was crucial for the permeability assay. Using the tape prevented the fluorescent vesicle suspension from entering into the metabolite inlet. The chip was then transferred under the microscope. A 1 mL plastic syringe (Becton Dickinson) was filled with the washing buffer and a second 1 mL syringe was filled with a 1 mM solution of the metabolite under investigation. Both syringes were connected to 23-gauge needles (Becton Dickinson) and Masterflex Transfer Tygon tubing with 0.5 mm inner and 1.5 mm outer diameter (Cole-Parmer Instrument). Next, the syringes were connected to a Nemesys pump controlled via the QmixElements software (Centoni). The tape was then removed from the metabolite inlet and the tubing containing the metabolite solution under investigation was inserted into the metabolite inlet while the metabolite solution was flowing at a rate of 0.5 µL/h. Next, the tubing containing the washing buffer was inserted into the washing buffer inlet while the buffer solution was flowing at a rate of 5 µL/h. These flow rates were then simultaneously increased at steps of 0.5 µL/h every 10 s up to 2 µL/h for the metabolite solution and at steps of 5 µL/h every 10 s up to 25 µL/h for the buffer solution (Figure 1A). These maximal flow rates were kept constant for 20 min to remove any free CF molecules from the microfluidic environment while the fluorescent vesicles remained confined in the coves (Figure 1B). Flowing the metabolite solution at a low rate (i.e. 2 µL/h) prevented the accumulation of free CF molecules in the metabolite inlet but did not affect the permeability assay since we obtained similar permeability traits in the absence or presence of this low flow rate. Next, the metabolite solution under investigation was delivered to the fluorescent vesicles in the coves by reducing the flow rate of the washing buffer from 25 µL/h to 1 µL/h and by increasing the flow rate of the metabolite solution from 2 µL/h to 25 µL/h (Figure 1C). Next, the chip was visually inspected by using a 20× 0.85 N.A. oil-immersion objective mounted on an inverted epifluorescence microscope (Olympus IX73) equipped with a sCMOS camera (Zyla 4.2, Andor, used at an

exposure time of 0.1s), a blue LED (CoolLED pE300white, used at 30% of its intensity) and a FITC filter. This setup allowed us to simultaneously image 12 coves, therefore the area of the chip that contained the higher number of vesicles trapped in the coves was chosen. An image of such an area was acquired immediately after increasing the metabolite solution flow rate and then at intervals of 30 s for 3 min. All experiments were performed at an intra- and extra-vesicle pH of 7.4, since pH changes are known to affect CF fluorescence intensity [69]. For each membrane mimic in Table S1, in order to account for the impact of both the delivery of the washing buffer solution and photobleaching on the intra-vesicle CF fluorescence signal, we performed separate control assays by connecting the metabolite inlet to a syringe containing the washing buffer solution instead of the metabolite solution. Apart from this modification, these control assays were carried out following the protocol described above for the microfluidic permeability assays. The intra-vesicle CF fluorescence consistently linearly decreased during the delivery of the washing buffer for all membrane mimics investigated and this information was used to provide a background signal for the corresponding microfluidic permeability assays (see Image and data analysis section below).

Image and data analysis

Images of the fluorescent vesicles for each membrane mimic trapped in the microfluidic coves during the 3 min delivery of each metabolite were imported in ImageJ to produce a temporal image stack [70] and analysed as follows to extract quantitative comparative information about the permeability traits of each membrane mimic to each metabolite. Only images of unilamellar vesicles were retained for analysis, whereas images of multilamellar vesicles were not taken forward. To obtain the single-vesicle temporal dependence of intra-vesicle fluorescence, for each image and each time point, a circle was drawn around each vesicle. A second circle of identical dimensions was drawn in an area 10 μm to the left of the vesicle. This allowed us to extract the mean CF fluorescence of each vesicle and the background around it at each time point, respectively. The background fluorescence was subtracted from the corresponding intra-vesicle fluorescence for each vesicle and each time point. Next, for each vesicle from all the background subtracted values, the initial intra-vesicle fluorescence value (at t=0) was subtracted. Next, these values were corrected to account for the impact of both the delivery of the washing buffer solution and photobleaching on the intra-vesicle CF fluorescence signal. To do so a correction factor was calculated from the microfluidic control assay data sets (see below), multiplied by each time value and added to the corresponding intra-vesicle fluorescence value (after the background and initial fluorescence value subtractions above). To obtain a correction factor for each membrane mimic, first we applied the image analysis protocol above to obtain the single-vesicle temporal dependence of intra-vesicle fluorescence values during the delivery of the washing buffer and subtract from these values the corresponding background and initial intra-vesicle fluorescence value. Second, we averaged these temporal dependences of corrected single-vesicle fluorescence values to obtain a mean temporal dependence for each membrane mimic during the delivery of the washing buffer. Finally, we fitted this mean temporal dependence to a linear regression with the intercept forced to zero and obtained the slope of the linear fluorescence decrease for each membrane mimic. These slope values were used as correction factors to calculate the permeability of each membrane mimic to each metabolite as described above. For some of the membrane mimic and metabolite pairs we noticed a minority of outliers (i.e. vesicles that became either much brighter or dimmer with respect to the majority of vesicles investigated during metabolite delivery, see for example Figure 2B). This heterogeneity is common when investigating membrane permeability both *in vitro* [40] and *in vivo* [39,43].

The permeability of each membrane mimic to each metabolite was measured in three independent experiments from three independent vesicle electroformations. Throughout the manuscript N indicates the number of single vesicles investigated for each membrane mimic and metabolite pair. N varies across different metabolite-experiments investigated since the number of vesicles trapped within the microfluidic coves of the chosen chip area varied. However, care was taken to obtain the same N for each metabolite-experiment across the different membrane mimics comparisons to ensure reliable statistical comparisons. In order to do so, when a statistical comparison was to be made between data sets of different N, corrected intra-vesicle fluorescence values were randomly selected from the data set that contained the higher N. Such statistical comparisons were carried out via two-tailed Mann-Whitney tests when comparing distributions of corrected intra-vesicle fluorescence values at t=3 min for two different lipid types (reported in Supplementary file 1) or Kruskal-Wallis one-way analysis of variance when comparing distributions of corrected intra-vesicle fluorescence values at t=3 min for more than two different lipid types (reported in Supplementary file 2). **** indicates a p-value < 0.0001, *** indicates a p-value < 0.001, ** indicates a p-value < 0.01, * indicates a p-value < 0.05, n.s. indicates a p-value > 0.05. All data analysis and statistical comparisons were carried out and plotted using GraphPad Prism 9.

In silico identification of prokaryotic transporter proteins

To characterize the transporter repertoires of bacterial and archaeal species in silico, we first assembled a collection of prokaryotic reference proteomes from UniProt (release 2021_03 [59]). To minimize taxonomic redundancy, a single proteome was selected per genus based on BUSCO completeness scores [71], resulting in 3,044 bacterial and 244 archaeal proteomes. Metagenomes from the bacterial candidate phyla radiation (CPR) were excluded due to their prevalence and lack of morphological information. To comprehensively identify transporter homologs, profile hidden Markov models (HMMs) derived from TCDB (Transporter Classification Database) protein families (termed tcDoms, downloaded 2 June 2021) were used to search each proteome using HMMER v3.1b2 ($E < 10^{-5}$, $incE < 10^{-5}$, $domE < 10^{-5}$) [59,72]. If multiple HMMs identified the same predicted protein, the protein was assigned to the family with the lower E-value. To improve the sensitivity of the HMMs, the hits from the initial HMM search were aligned using MAFFT v7.471 (-auto), trimmed with a gap-threshold of 10% using trimAl v1.4, and the resulting alignments were used to generate new HMMs [59,73]. Using the second iteration HMMs, another search was conducted as above, producing the final set of identified proteins. To reduce the potential effects of taxon sampling and dataset bias, prokaryotic taxa were grouped into their respective orders based on NCBI Taxonomy classifications [74]. Transporter abundance was then interpreted as the median number of transporters assigned to a given TCDB family, normalized by the total number of proteins encoded by each taxa, across each order. The resulting distribution was visualized in R v4.0.2 and hierarchical clustering was done using euclidean distances and the Ward.D2 clustering method implemented by pheatmap (https://mran.microsoft.com/snapshot/2018-08-31/web/packages/pheatmap/pheatmap.pdf). The differential abundance of individual transporter families was assessed by comparing archaeal and monoderm transporter abundances (given their morphological similarities) using Wilcoxon tests after Bonferroni correction.

To identify putative archaeal transporter families undetected by the TCDB HMMs, we clustered archaeal proteomes into protein families using the Markov clustering algorithm (I=1.4) based on pairwise BLASTp searches conducted using Diamond v2.0.9.147 ($E < 10^{-5}$, query coverage > 50%, -max-target-seqs $=10^5$, --more-sensitive search option) [75,76]. Transmembrane (TM) domains were then predicted for each

archaeal protein using Phobius and the median number of TM domains was determined for each protein family [77]. Those families with representation in at least five archaeal species and with a median of at least four TM domains were identified and annotated using eggNOG mapper v2.1.2 [78]. TM domain-containing protein families were classified as putative transporters if they were annotated with PFAM domains associated with transporter function (e.g., all transporter and channel-associated domains) [79]. Bacterial homologs of archaeal protein families were detected using Diamond BLASTp by searching the bacterial reference proteomes with each protein family ($E < 10^{-20}$, query coverage > 50%). To compare TM domain lengths and amino acid composition in Archaea and Bacteria, TM domains were predicted from archaeal and bacterial proteins using Phobius and their length and composition was assessed using BioPython (https://academic.oup.com/bioinformatics/article/25/11/1422/330687?login=true).

FUNDING

U.L., G.G., Z.K. and D.S.M. were supported via a Gordon and Betty Moore Foundation Marine Microbiology Initiative grant (GBMF5514) awarded to T.A.R., A.E.S. and S.P.. U.L. was also supported through a BBSRC responsive mode grant (BB/V008021/1) awarded to S.P.. N.A.T.I. was supported by a Junior Research Fellowship from Merton College, University of Oxford. S.P. and T.A.R.'s work in this area was also supported by a Marie Skłodowska-Curie project SINGEK (H2020-MSCA-ITN-2015-675752). M.T. and S.-V.A. were supported by the VW foundation by a Life? Grant (Life? Az 96727).

REFERENCES

1. Lohrmann R, Orgel LE. Prebiotic activation processes. Nature. 1973;244: 418–420. doi:10.1038/244418a0
2. Woese CR, Fox GE. Phylogenetic structure of the prokaryotic domain: The primary kingdoms. Proc Natl Acad Sci U S A. 1977;74: 5088–5090. doi:10.1073/pnas.74.11.5088
3. Woese CR, Kandler O, Wheelis ML. Towards a natural system of organisms: Proposal for the domains Archaea, Bacteria, and Eucarya. Proc Natl Acad Sci U S A. 1990;87: 4576–4579. doi:10.1073/pnas.87.12.4576
4. Baldauf SL, Palmer JD, Doolittle WF. The root of the universal tree and the origin of eukaryotes based on elongation factor phylogeny. Proc Natl Acad Sci U S A. 1996;93: 7749–7754. doi:10.1073/pnas.93.15.7749
5. Brown JR, Doolittle WF. Root of the universal tree of life based on ancient aminoacyl-tRNA synthetase gene duplications. Proc Natl Acad Sci U S A. 1995;92: 2441–2445. doi:10.1073/pnas.92.7.2441
6. Fournier GP, Gogarten JP. Rooting the ribosomal tree of life. Mol Biol Evol. 2010;27: 1792–1801. doi:10.1093/molbev/msq057
7. Coleman GA, Pancost RD, Williams TA. GBE Investigating the Origins of Membrane Phospholipid Biosynthesis Genes Using Outgroup-Free Rooting. Genome Biol Evol. 2019;11: 883–898. doi:10.1093/gbe/evz034
8. Williams TJ, Allen M, Tschitschko B, Cavicchioli R. Glycerol metabolism of haloarchaea. Environ Microbiol. 2017;19: 864–877. doi:10.1111/1462-2920.13580
9. Williams TA, Foster PG, Cox CJ, Embley TM. An archaeal origin of eukaryotes supports only two primary domains of life. Nature. 2013;504: 231–236. doi:10.1038/nature12779

10. Esko J, Doering T, Raetz C. Eubacteria and Archaea. 2nd ed. In: Varki A, Cummings RD, Esko JD, et al. editors. E of G, editor. Cold Spring Harbor (NY): Cold Spring Harbor Laboratory Press; 2009.
11. Kelman Z, Hurwitz J. Structural lessons in DNA replication from. Nat Struct Biol. 2003;10: 148.
12. Mattiroli F, Bhattacharyya S, Dyer PN, White AE, Sandman K, Burkhart BW, et al. Structure of histone-based chromatin in Archaea. Science (80-). 2017;357: 609–612. doi:10.1126/science.aaj1849
13. Lombard J, López-García P, Moreira D. The early evolution of lipid membranes and the three domains of life. Nat Rev Microbiol. 2012;10: 507–515. doi:10.1038/nrmicro2815
14. Sojo V. Why the Lipid Divide? Membrane Proteins as Drivers of the Split between the Lipids of the Three Domains of Life. BioEssays. 2019;41: 1–6. doi:10.1002/bies.201800251
15. Eme L, Spang A, Lombard J, Stairs CW, Ettema TJG. Archaea and the origin of eukaryotes. Nat Rev Microbiol. 2017;15: 711–723. doi:10.1038/nrmicro.2017.133
16. Mathai JC, Sprott GD, Zeidel ML. Molecular Mechanisms of Water and Solute Transport across Archaebacterial Lipid Membranes *. J Biol Chem. 2001;276: 27266–27271. doi:10.1074/jbc.M103265200
17. Sinensky M. Homeoviscous adaptation: a homeostatic process that regulates the viscosity of membrane lipids in Escherichia coli. Proc Natl Acad Sci U S A. 1974;71: 522–525. doi:10.1073/pnas.71.2.522
18. Siliakus MF, van der Oost J, Kengen SWM. Adaptations of archaeal and bacterial membranes to variations in temperature, pH and pressure. Extremophiles. 2017;21: 651–670. doi:10.1007/s00792-017-0939-x
19. Sojo V, Pomiankowski A, Lane N. A Bioenergetic Basis for Membrane Divergence in Archaea and Bacteria. PLoS Biol. 2014;12: e1001926. doi:10.1371/journal.pbio.1001926
20. Adamala K, Szostak JW. Competition between model protocells driven by an encapsulated catalyst. Nat Chem. 2013;5: 495–501. doi:10.1038/nchem.1650
21. Budin I, Szostak JW. Physical effects underlying the transition from primitive to modern cell membranes. Proc Natl Acad Sci U S A. 2011;108: 5249–5254. doi:10.1073/pnas.1100498108
22. Shimada H, Yamagishi A. Stability of heterochiral hybrid membrane made of bacterial sn -G3P lipids and archaeal sn -G1P lipids. Biochemistry. 2011;50: 4114–4120. doi:10.1021/bi200172d
23. Blain JC, Szostak JW. Progress toward synthetic cells. Annu Rev Biochem. 2014;83: 615–640. doi:10.1146/annurev-biochem-080411-124036
24. Jordan SF, Nee E, Lane N. Isoprenoids enhance the stability of fatty acid membranes at the emergence of life potentially leading to an early lipid divide. Interface Focus. 2019;9. doi:10.1098/rsfs.2019.0067
25. Morowitz HJ, Heinz B, Deamer DW. The chemical logic of a minimum protocell. Orig Life Evol Biosph. 1988;18: 281–287. doi:10.1007/BF01804674
26. Khvorova A, Kwak YG, Tamkun M, Majerfeld I, Yarus M. RNAs that bind and change the permeability of phospholipid membranes. Proc Natl Acad Sci U S A. 1999;96: 10649–10654. doi:10.1073/pnas.96.19.10649
27. Mathai JC, Tristram-Nagle S, Nagle JF, Zeidel ML. Structural determinants of water permeability through the lipid membrane. J Gen Physiol. 2008;131: 69–76. doi:10.1085/jgp.200709848
28. Valentine DL. Adaptations to energy stress dictate the ecology and evolution of the Archaea. Nat Rev

Microbiol. 2007;5: 1070–1077.

29. Frallicciardi J, Melcr J, Siginou P, Marrink SJ, Poolman B. Membrane thickness, lipid phase and sterol type are determining factors in the permeability of membranes to small solutes. Nat Commun. 2022;13: 1–12. doi:10.1038/s41467-022-29272-x
30. Mansy SS, Schrum JP, Krishnamurthy M, Tobé S, Treco DA, Szostak JW. Template-directed synthesis of a genetic polymer in a model protocell. Nature. 2008;454: 122–125. doi:10.1038/nature07018
31. Yamauchi K, Doi K, Yoshida Y, Kinoshita M. Archaebacterial lipids: highly proton-impermeable membranes from 1,2-diphytanyl-sn-glycero-3-phosphocoline. BBA - Biomembr. 1993;1146: 178–182. doi:10.1016/0005-2736(93)90353-2
32. Van De Vossenberg JLCM, Ubbink-Kok T, Elferink MGL, Driessen AJM, Konings WN. Ion permeability of the cytoplasmic membrane limits the maximum growth temperature of bacteria and archaea. Mol Microbiol. 1995;18: 925–932. doi:10.1111/j.1365-2958.1995.18050925.x
33. Bozdaganyan ME, Lokhmatikov A V., Voskoboynikova N, Cherepanov DA, Steinhoff HJ, Shaitan K V., et al. Proton leakage across lipid bilayers: Oxygen atoms of phospholipid ester linkers align water molecules into transmembrane water wires. Biochim Biophys Acta - Bioenerg. 2019;1860: 439–451. doi:10.1016/j.bbabio.2019.03.001
34. Ude J, Tripathi V, Buyck JM, Söderholm S, Cunrath O, Fanous J, et al. Outer membrane permeability: Antimicrobials and diverse nutrients bypass porins in Pseudomonas aeruginosa. Proc Natl Acad Sci U S A. 2021;118: 1–8. doi:10.1073/pnas.2107644118
35. Cama J, Schaich M, Al Nahas K, Hernández-Ainsa S, Pagliara S, Keyser UF. Direct Optofluidic Measurement of the Lipid Permeability of Fluoroquinolones. Sci Rep. 2016;6: 32824. doi:10.1038/srep32824
36. Sacerdote MG, Szostak JW. Semipermeable lipid bilayers exhibit diastereoselectivity favoring ribose. Proc Natl Acad Sci U S A. 2005;102: 6004–6008. doi:10.1073/pnas.0408440102
37. Orsi M, Sanderson WE, Essex JW. Permeability of small molecules through a lipid bilayer: A multiscale simulation study. J Phys Chem B. 2009;113: 12019–12029. doi:10.1021/jp903248s
38. Hu J, Cochrane WG, Jones AX, Blackmond DG, Paegel BM. Chiral lipid bilayers are enantioselectively permeable. Nat Chem. 2021;13: 786–791. doi:10.1038/s41557-021-00708-z
39. Lapinska U, Glover G, Capilla-lasheras P, Young AJ, Pagliara S. Bacterial ageing in the absence of external stressors. Philos Trans R Soc B Biol Sci. 2019;374: 20180442.
40. Cama J, Nahas K Al, Fletcher M, Hammond K, Maxim G. An ultrasensitive microfluidic approach reveals correlations between the physico-chemical and biological activity of experimental peptide antibiotics. Sci Rep. 2022;12: 4005. doi:10.1038/s41598-022-07973-z
41. Łapińska U, Voliotis M, Lee KK, Campey A, Stone MRL, Phetsang W, et al. Fast bacterial growth reduces antibiotic accumulation and efficacy. Elife. 2022;11: e74062.
42. Glover G, Voliotis M, Łapińska U, Invergo BM, Soanes D, O'Neill P, et al. Nutrient and salt depletion synergistically boosts glucose metabolism in individual Escherichia coli cells. Commun Biol. 2022;5: 385.
43. Stone MRL, Łapińska U, Pagliara S, Masi M, Blanchfield JT, Cooper MA, et al. Fluorescent macrolide probes – synthesis and use in evaluation of bacterial resistance. RSC Chem Biol. 2020;1: 395–404. doi:10.1039/d0cb00118j

44. Komatsu H, Chong PLG. Low permeability of liposomal membranes composed of bipolar tetraether lipids from thermoacidophilic archaebacterium Sulfolobus acidocaldarius. Biochemistry. 1998;37: 107–115. doi:10.1021/bi972163e
45. Sprott GD, Larocque S, Cadotte N, Dicaire CJ, McGee M, Brisson JR. Novel polar lipids of halophilic eubacterium Planococcus H8 and archaeon Haloferax volcanii. Biochim Biophys Acta - Mol Cell Biol Lipids. 2003;1633: 179–188. doi:10.1016/j.bbalip.2003.08.001
46. Sprott GD, Agnew BJ, Patel GB. Structural features of ether lipids in the archaeobacterial thermophiles Pyrococcus furiosus, Methanopyrus kandleri, Methanothermus fervidus, and Sulfolobus acidocaldarius. Can J Microbiol. 1997;43: 467–476. doi:https://doi.org/10.1139/m97-066
47. Poger D, Caron B, Mark AE. Effect of methyl-branched fatty acids on the structure of lipid bilayers. J Phys Chem B. 2014;118: 13838–13848. doi:10.1021/jp503910r
48. Kara S, Afonin S, Babii O, Tkachenko AN, Komarov I V., Ulrich AS. Diphytanoyl lipids as model systems for studying membrane-active peptides. Biochim Biophys Acta - Biomembr. 2017;1859: 1828–1837. doi:10.1016/j.bbamem.2017.06.003
49. Paula S, Volkov AG, Deamer DW. Permeation of halide anions through phospholipid bilayers occurs by the solubility-diffusion mechanism. Biophys J. 1998;74: 319–327. doi:10.1016/S0006-3495(98)77789-6
50. Jain S, Caforio A, Driessen AJM. Biosynthesis of archaeal membrane ether lipids. Front Microbiol. 2014;5: 1–16. doi:10.3389/fmicb.2014.00641
51. Elling FJ, Könneke M, Nicol GW, Stieglmeier M, Bayer B, Spieck E, et al. Chemotaxonomic characterisation of the thaumarchaeal lipidome. Environ Microbiol. 2017;19: 2681–2700. doi:10.1111/1462-2920.13759
52. Bauersachs T, Weidenbach K, Schmitz RA, Schwark L. Distribution of glycerol ether lipids in halophilic, methanogenic and hyperthermophilic archaea. Org Geochem. 2015;83–84: 101–108. doi:10.1016/j.orggeochem.2015.03.009
53. Chong PLG, Ayesa U, Prakash Daswani V, Hur EC. On physical properties of tetraether lipid membranes: Effects of cyclopentane rings. Archaea. 2012;2012. doi:10.1155/2012/138439
54. Cama J, Chimerel C, Pagliara S, Javer A, Keyser UF. A label-free microfluidic assay to quantitatively study antibiotic diffusion through lipid membranes. Lab Chip. 2014;14: 2303–8. doi:10.1039/c4lc00217b
55. Blicher A, Wodzinska K, Fidorra M, Winterhalter M, Heimburg T. The temperature dependence of lipid membrane permeability, its quantized nature, and the influence of anesthetics. Biophys J. 2009;96: 4581–4591. doi:10.1016/j.bpj.2009.01.062
56. Caforio A, Siliakus MF, Exterkate M, Jain S, Jumde VR, Andringa RLH, et al. Converting Escherichia coli into an archaebacterium with a hybrid heterochiral membrane. Proc Natl Acad Sci U S A. 2018;115: 3704–3709. doi:10.1073/pnas.1721604115
57. Martin W, Hoffmeister M, Rotte C, Henze K. An overview of endosymbiotic models for the origins of eukaryotes, their ATP-producing organelles (mitochondria and hydrogenosomes), and their heterotrophic lifestyle. Biol Chem. 2001;382: 1521–1539. doi:10.1515/BC.2001.187
58. Martin William, Miklós M. The hydrogen hypothesis for the first eukaryote. Nature. 1998;392: 37–41.
59. Saier MH, Reddy VS, Moreno-Hagelsieb G, Hendargo KJ, Zhang Y, Iddamsetty V, et al. The transporter classification database (TCDB): 2021 update. Nucleic Acids Res. 2021;49: D461–D467.

doi:10.1093/nar/gkaa1004

60. Eguchi T, Arakawa K, Terachi T, Kakinuma K. Total synthesis of archaeal 36-membered macrocyclic diether lipid. J Org Chem. 1997;62: 1924–1933. doi:10.1021/jo962327h
61. Balleza D, Garcia-Arribas AB, Sot J, Ruiz-Mirazo K, Goñi FM. Ether- Versus ester-linked phospholipid bilayers containing either linear or branched apolar chains. Biophys J. 2014;107: 1364–1374. doi:10.1016/j.bpj.2014.07.036
62. Tourte M, Schaeffer P, Grossi V, Oger PM. Functionalized Membrane Domains: An Ancestral Feature of Archaea? Front Microbiol. 2020;11: 1–14. doi:10.3389/fmicb.2020.00526
63. Locatelli E, Pierno M, Baldovin F, Orlandini E, Tan Y, Pagliara S. Single-File Escape of Colloidal Particles from Microfluidic Channels. Phys Rev Lett. 2016;117: 038001. doi:10.1103/PhysRevLett.117.038001
64. Lapinska U, Saar KL, Yates E, Herling T, Muller T, Challa PK, et al. Gradient-free determination of isoelectric points of proteins on chip. Phys Chem Chem Phys. 2017;19: 23060–23067. doi:10.1039/c7cp01503h
65. Goode O, Smith A, Łapińska U, Attrill E, Carr A, Metz J, et al. Heterologous Protein Expression Favors the Formation of Protein Aggregates in Persister and Viable but Nonculturable Bacteria´. ACS Infect Dis. 2021;7: 1848. doi:10.1021/acsinfecdis.1c00154
66. Cama J, Pagliara S. Microfluidic Single-Cell Phenotyping of the Activity of Peptide-Based Antimicrobials. Polypeptide Materials: Methods and Protocols Methods in Molecular Biology. 2021. pp. 237–253. doi:10.2307/j.ctt1ffjgqc.20
67. Di Carlo D, Aghdam N, Lee LP. Single-cell enzyme concentrations, kinetics, and inhibition analysis using high-density hydrodynamic cell isolation arrays. Anal Chem. 2006;78: 4925–4930. doi:10.1021/ac060541s
68. Hodgson AC, Verstreken CM, Fisher CL, Keyser UF, Pagliara S, Chalut KJ. A microfluidic device for characterizing nuclear deformations. Lab Chip. 2017;17: 805–813. doi:10.1039/C6LC01308B
69. Sjöback R, Nygren J, Kubista M. Absorption and fluorescence properties of fluorescein. Spectrochim Acta Part A Mol Spectrosc. 1995;51. doi:10.1016/0584-8539(95)01421-P
70. Goode O, Smith A, Zarkan A, Cama J, Invergo BM, Belgami D, et al. Persister Escherichia coli Cells Have a Lower Intracellular pH than Susceptible Cells but Maintain Their pH in Response to Antibiotic Treatment. MBio. 2021;12: e00909-21.
71. Simão FA, Waterhouse RM, Ioannidis P, Kriventseva E V., Zdobnov EM. BUSCO: Assessing genome assembly and annotation completeness with single-copy orthologs. Bioinformatics. 2015;31: 3210–3212. doi:10.1093/bioinformatics/btv351
72. Mistry J, Finn RD, Eddy SR, Bateman A, Punta M. Challenges in homology search: HMMER3 and convergent evolution of coiled-coil regions. Nucleic Acids Res. 2013;41. doi:10.1093/nar/gkt263
73. Capella-Gutiérrez S, Silla-Martínez JM, Gabaldón T. trimAl: A tool for automated alignment trimming in large-scale phylogenetic analyses. Bioinformatics. 2009;25: 1972–1973. doi:10.1093/bioinformatics/btp348
74. Federhen S. The NCBI Taxonomy database. Nucleic Acids Res. 2012;40: 136–143. doi:10.1093/nar/gkr1178
75. Buchfink B, Reuter K, Drost HG. Sensitive protein alignments at tree-of-life scale using DIAMOND. Nat Methods. 2021;18: 366–368. doi:10.1038/s41592-021-01101-x

76. Enright AJ, Van Dongen S, Ouzounis CA. An efficient algorithm for large-scale detection of protein families. Nucleic Acids Res. 2002;30: 1575–1584. doi:10.1093/nar/30.7.1575

77. Käll L, Krogh A, Sonnhammer ELL. A combined transmembrane topology and signal peptide prediction method. J Mol Biol. 2004;338: 1027–1036. doi:10.1016/j.jmb.2004.03.016

78. Huerta-Cepas J, Forslund K, Coelho LP, Szklarczyk D, Jensen LJ, Von Mering C, et al. Fast genome-wide functional annotation through orthology assignment by eggNOG-mapper. Mol Biol Evol. 2017;34: 2115–2122. doi:10.1093/molbev/msx148

79. El-Gebali S, Mistry J, Bateman A, Eddy SR, Luciani A, Potter SC, et al. The Pfam protein families database in 2019. Nucleic Acids Res. 2019;47: D427–D432. doi:10.1093/nar/gky995

FIGURES

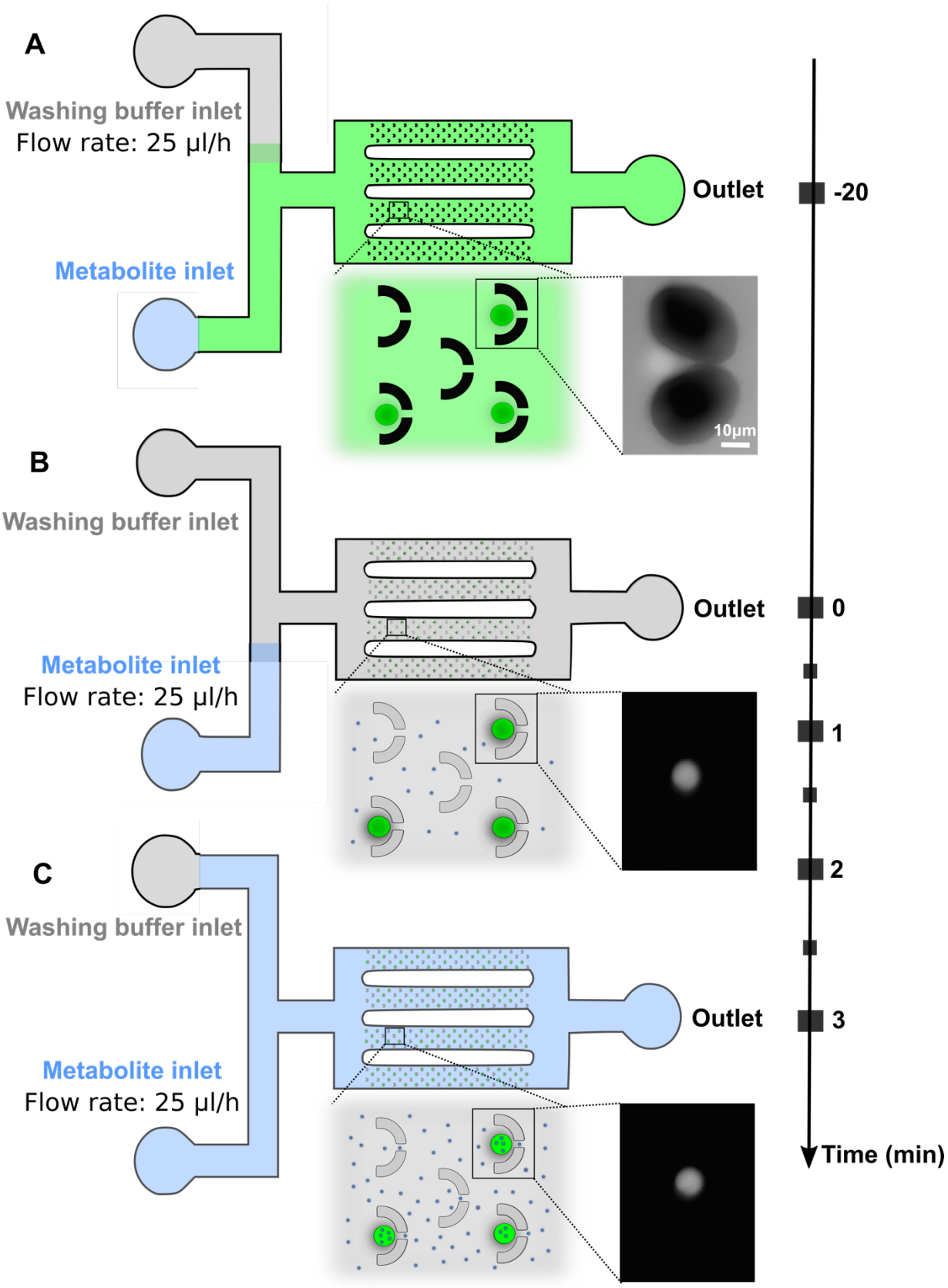

Figure 1. Schematics illustrating the microfluidic approach used to study membrane permeability. **a)** Vesicles (green circles) loaded into the fluidic device (at t=-20 min) display an intracellular carboxyfluorescein (CF) concentration that is similar to the extracellular CF concentration, thus vesicles confined in the fluidic coves appear as bright as the extracellular environment, as illustrated by the micrograph. Free CF molecules

are removed from the microfluidic environment around the vesicles by applying a flow rate of 25 µL/h from the washing buffer inlet for 20 minutes. **b)** At t=0 min vesicles appear bright on a dark background as shown in the micrograph. The metabolite (small blue circles) under investigation is delivered to the vesicles by applying a flow rate of 25 µL/h from the metabolite inlet for 3 minutes. **c)** The metabolite accumulates within the vesicles if their membrane is permeable to the metabolite.

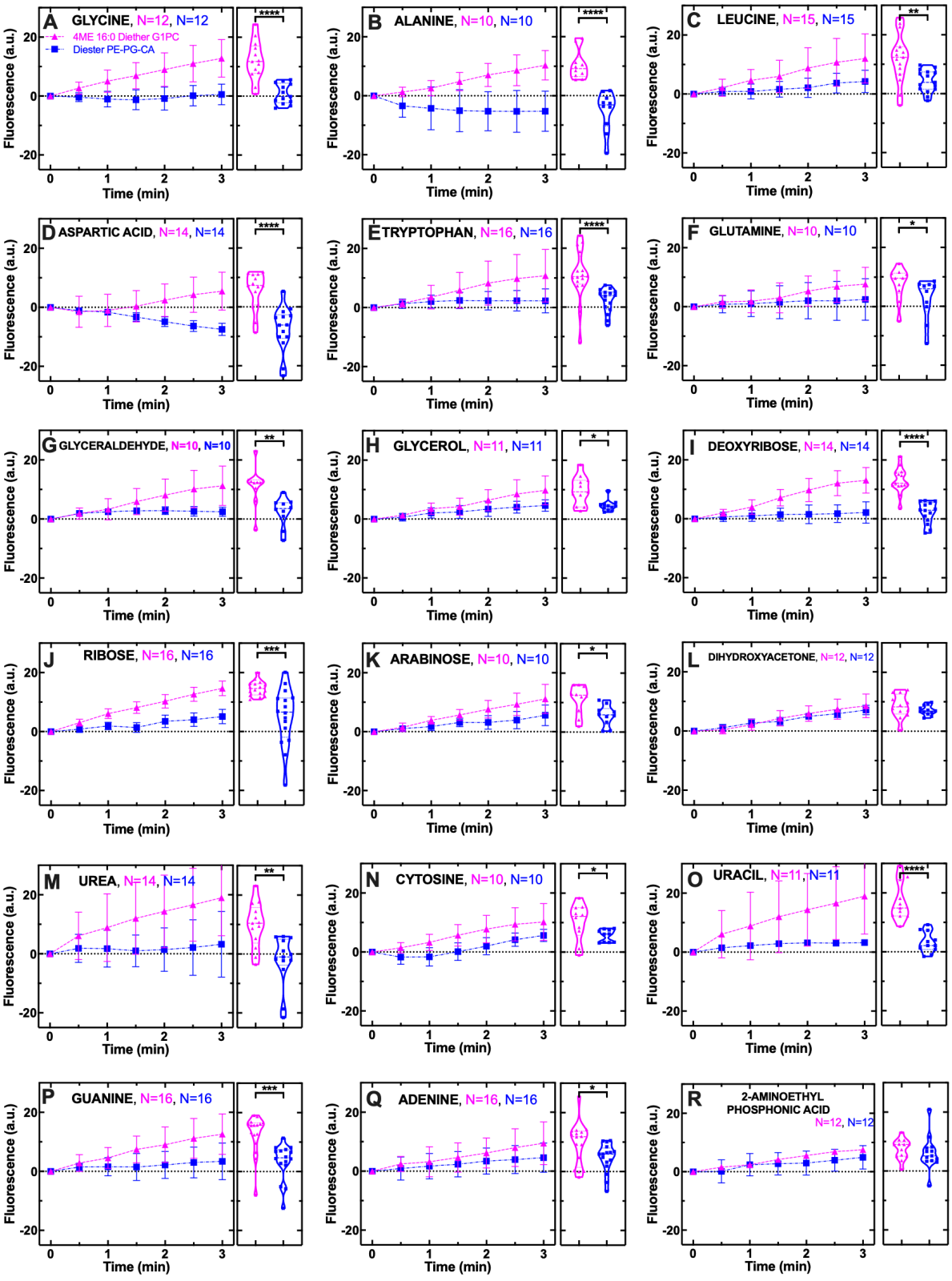

Figure 2. Archaeal 4ME diether G1PC vesicles are consistently more permeable to a range of metabolites than bacterial diester G3PE-PG-CA vesicles. Temporal dependence of average CF fluorescence in archaeal 4ME diether G1PC (magenta triangles) and bacterial diester G3PE-PG-CA vesicles (blue squares) during the exposure to 1 mM of variant metabolites delivered to the microfluidic coves. Mean (symbols) and standard deviation (error bars) were calculated from at least 10 single-vesicle measurements across three independent experiments. Lines are guides for the eye. N is the number of single vesicles investigated for each metabolite exposure and each type of vesicles (magenta and blue for archaeal 4ME diether G1PC and bacterial diester G3PE-PG-CA vesicles, respectively). N varies across different metabolite-experiments investigated due to technical constraints (see Methods). However, care has been taken to obtain the same N for each metabolite-experiment across the two different types of vesicles to ensure reliable statistical comparisons. Such comparisons have been carried out via two-tailed Mann-Whitney tests between the distributions of CF fluorescence values at t=3 min for archaeal 4ME diether G1PC and bacterial diester G3PE-PG-CA vesicles. ****: p-value < 0.0001, ***: p-value < 0.001, **: p-value < 0.01, *: p-value < 0.05 and are shown with corresponding violin plots next to each time-course graph. The lipids used for creating archaeal 4ME diether G1PC and bacterial diester G3PE-PG-CA vesicles are lipids 1 and 2, respectively, in Table S1.

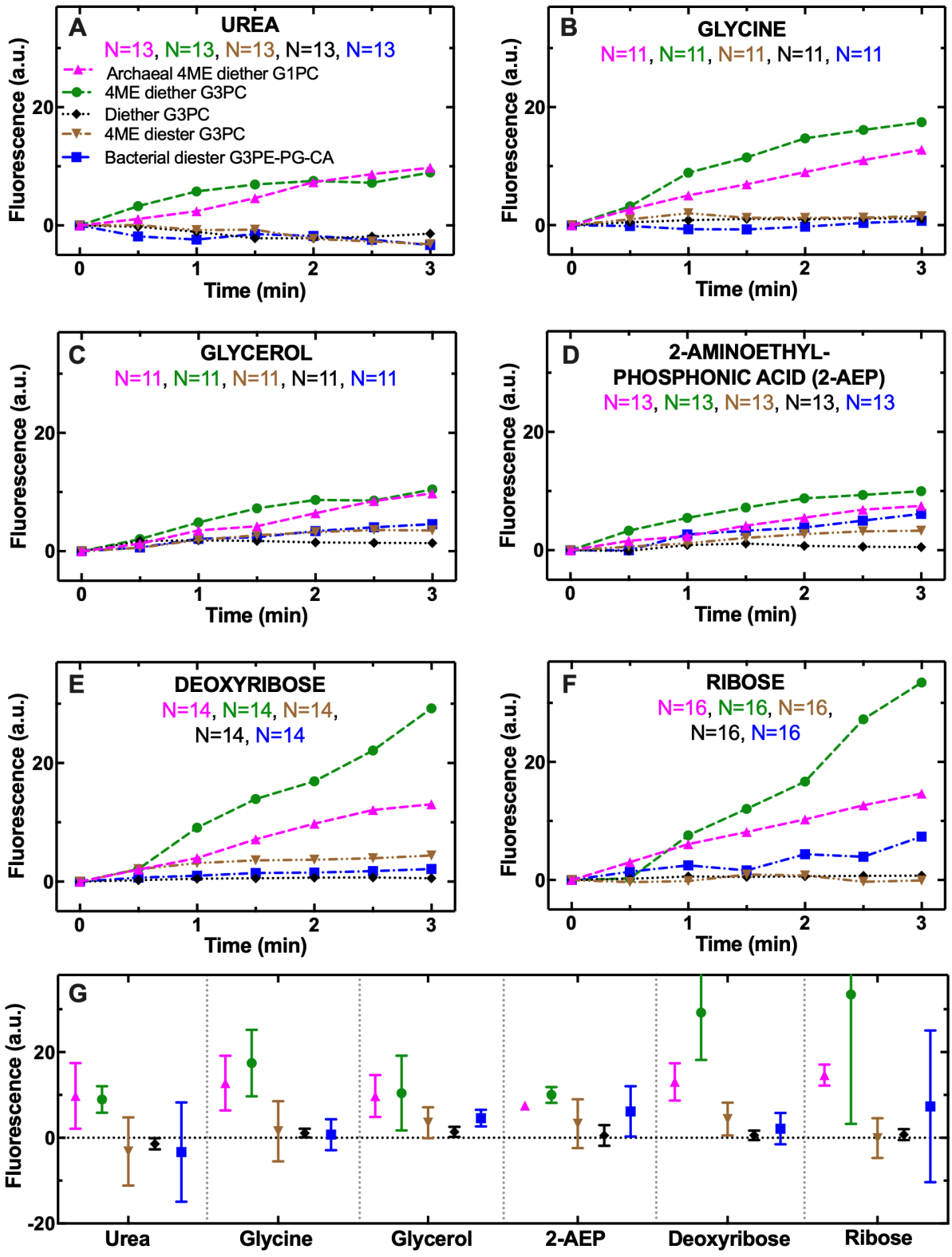

Figure 3. Chain branching and ether bond have profound implications on archaeal membrane permeability to small metabolites. Temporal dependence of average CF fluorescence in archaeal 4ME diether G1PC (magenta upward triangles), bacterial diester G3PE-PG-CA (blue squares), 4ME diether G3PC (green circles), 16:0 Diether G3PC (black diamonds), or 4ME 16:0 Diester G3PC (brown downward triangles) vesicles during the exposure to 1 mM **a)** urea, **b)** glycine, **c)** glycerol, **d)** 2-aminoethyl phosphonic acid, **e)** deoxyribose or **f)** ribose delivered to the vesicles at t=0. These substrates were chosen as previous analyses

demonstrate that these had key differences in permeability characteristics. Data for archaeal 4ME diether G1PC and bacterial diester G3PE-PG-CA vesicles are reproduced from Figure 2 for comparison purposes. Means (symbols) were calculated from at least 10 single-vesicle measurements across 3 independent experiments. Due to the large overlaps between the measurements obtained with the different vesicle types, standard deviations and single-vesicle measurements are not reported for clarity. Lines are guides for the eye. Mean and standard deviations measured at t=3 min and statistical comparisons carried out via Kruskal-Wallis one-way analysis of variance between the distributions of CF fluorescence values at t=3 min for each type of vesicle pair are reported in **g)** and in Supplementary file 1. ****: p-value < 0.0001, ***: p-value < 0.001, **: p-value < 0.01, *: p-value < 0.05. N is the number of single vesicles investigated for each metabolite and each lipid type. N varies across different metabolite-experiments investigated due to technical constraints (see Methods). However, care has been taken to obtain the same N for each metabolite-experiment across each pair of lipid type to ensure reliable statistical comparisons. The lipids used for creating archaeal 4ME diether G1PC, bacterial diester G3PE-PG-CA, 4ME diether G3PC, 16:0 Diether G3PC, or 4ME 16:0 Diester G3PC vesicles are lipids 1, 2, 3, 4 and 5, respectively, in Table S1.

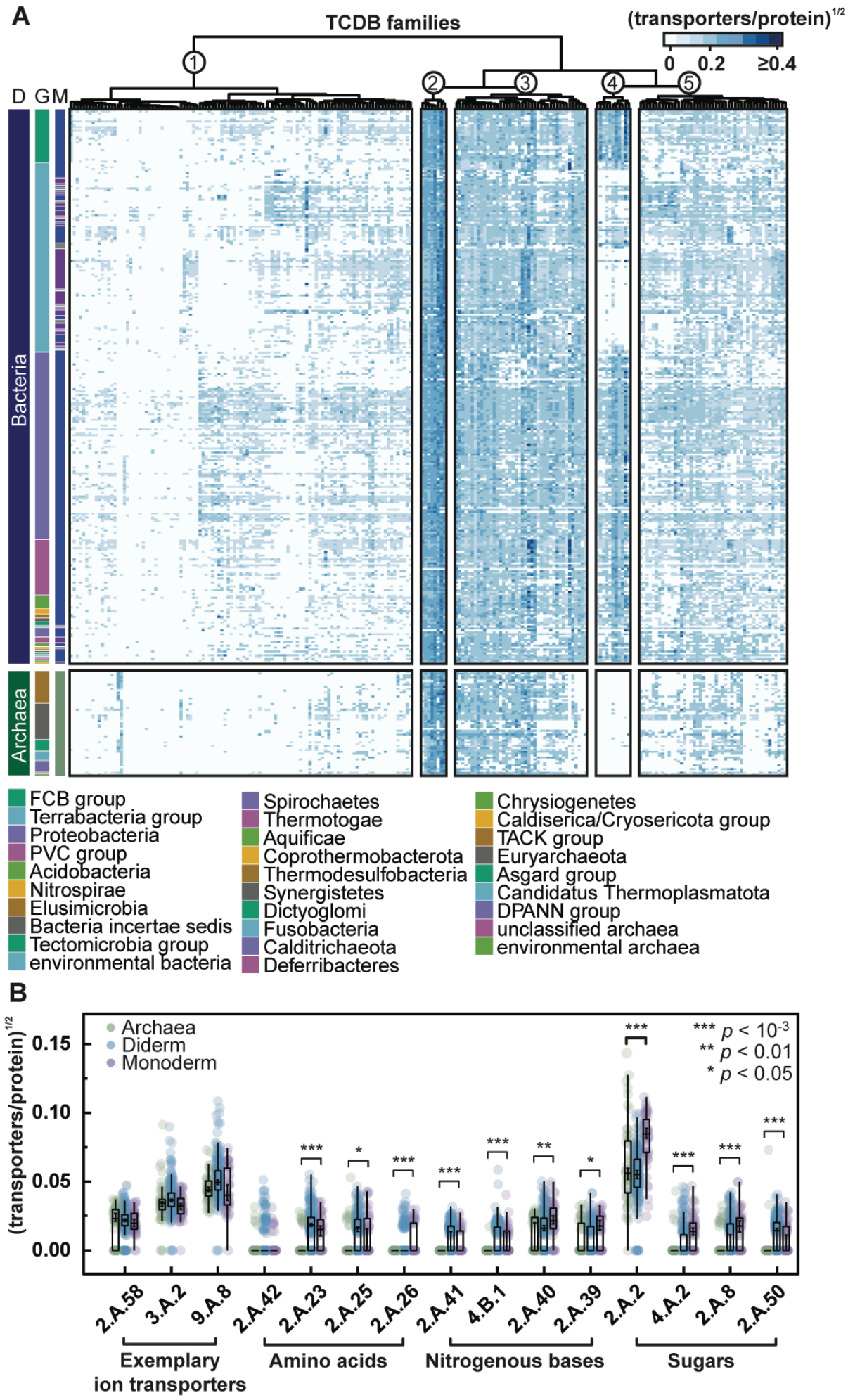

Figure 4. Archaea feature reduced transporter repertoires relative to Bacteria. a) Heatmap showing transporter repertoires in Archaea and Bacteria, where each row and column represent a prokaryotic order and TCDB transporter family, respectively. Heat map values represent the median number of transporters normalized by total protein count for every taxon across each prokaryotic order after a square root transformation to account for bias sampling of some taxa. The domain (D), group (G), and membrane morphology (M: where blue, purple, and grey, represent diderms, monoderms, and unknown membrane morphology, respectively) of each order is noted. TCDB families were grouped by hierarchical clustering based on transporter abundance using euclidean distances and the Ward.D2 clustering method. Taxonomy was based on NCBI Taxonomy classifications. **b)** Individual comparisons of transporter families in Archaea, monoderms, and diderms. All transporter families predicted to translocate amino acids, nitrogenous bases, and sugars are shown, alongside three exemplary ion transporter families from Cluster 2. Comparisons were made using Wilcoxon tests and Bonferroni corrected *p* values are shown. To assess taxon sampling bias, bootstrap-estimated 90% confidence intervals (n=1,000) of the median are displayed over each boxplot median based on random sampling of prokaryotic orders with replacement.

SUPPLEMENTARY FIGURES

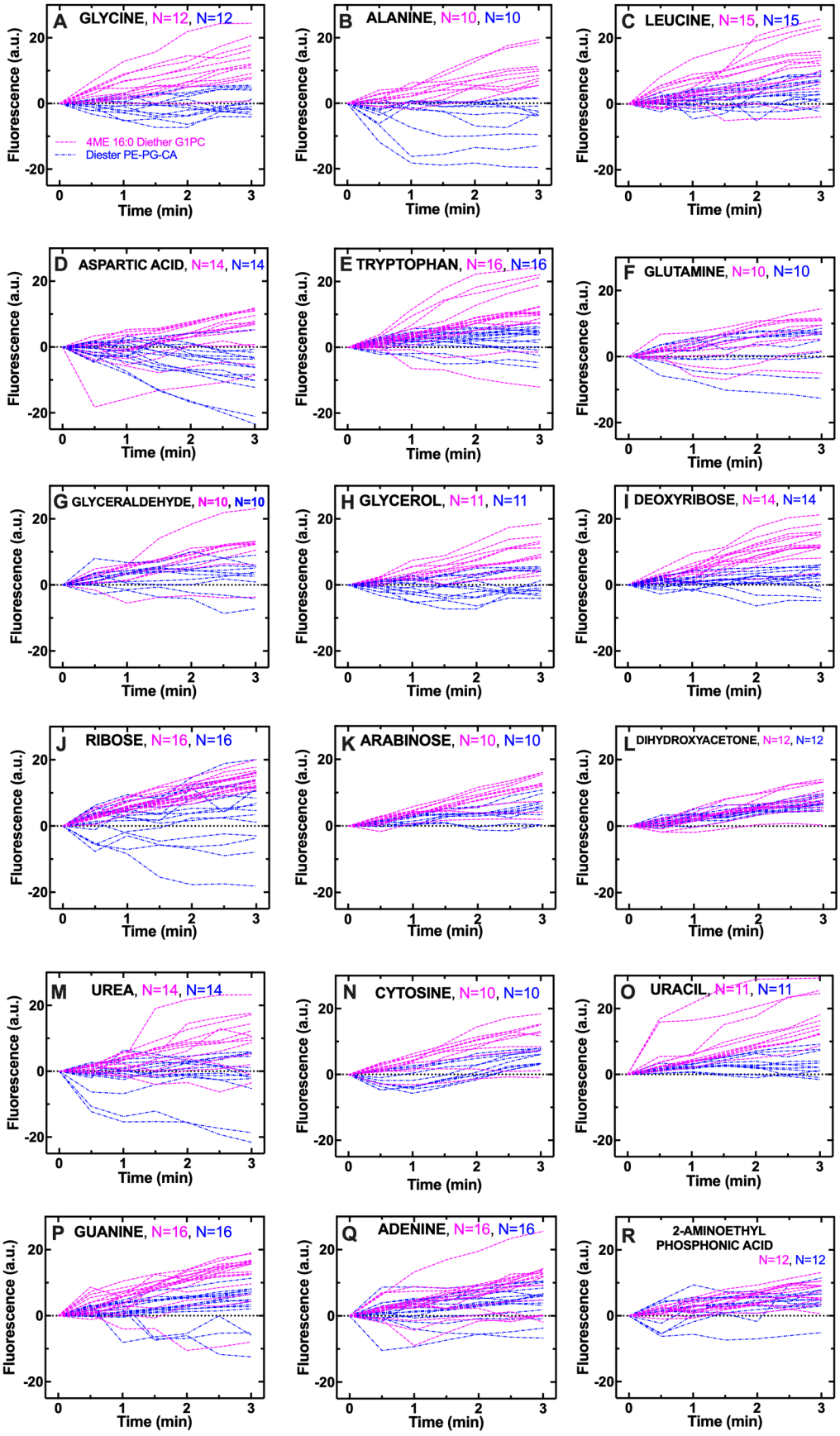

Figure S1. Individual archaeal 4ME diether G1PC vesicles are consistently more permeable to a range of metabolites than bacterial diester G3PE-PG-CA vesicles. Temporal dependence of CF fluorescence in

individual archaeal 4ME diether G1PC (magenta dashed lines) and bacterial diester G3PE-PG-CA vesicles (blue dashed-dotted lines) during the exposure to 1 mM of variant metabolites delivered to the microfluidic coves. N is the number of single vesicles investigated for each metabolite exposure and each type of vesicles (magenta and blue for archaeal 4ME diether G1PC and bacterial diester G3PE-PG-CA vesicles, respectively). N varies across different metabolite-experiments investigated due to technical constraints (see Methods). However, care has been taken to obtain the same N for each metabolite-experiment across the two different types of vesicles to ensure reliable statistical comparisons. The lipids used for creating archaeal 4ME diether G1PC and bacterial diester G3PE-PG-CA vesicles are lipids 1 and 2, respectively, in Table S1.

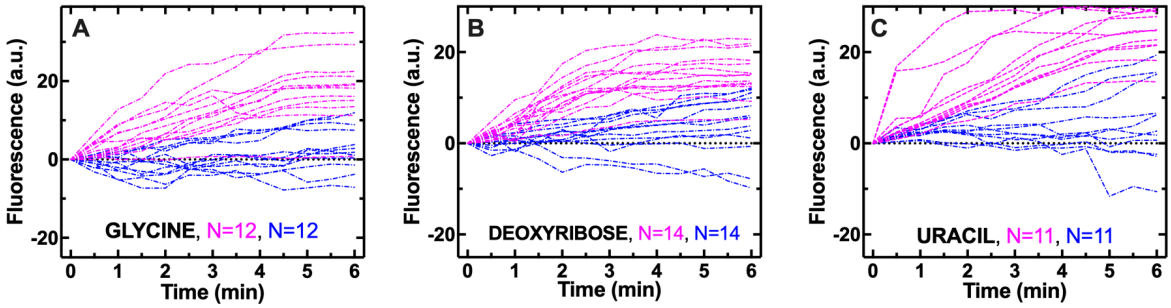

Figure S2. Individual archaeal 4ME diether G1PC vesicles remain more permeable than bacterial diester G3PE-PG-CA vesicles over longer timescales. Temporal dependence of CF fluorescence in individual archaeal 4ME diether G1PC (magenta dashed lines) and bacterial diester G3PE-PG-CA vesicles (blue dashed-dotted lines) during the exposure to 1 mM of variant glycine, deoxyribose or uracil delivered to the microfluidic coves. Individual archaeal 4ME diether G1PC vesicles remain more permeable than bacterial diester G3PE-PG-CA vesicles over a 6 minute exposure to metabolites.

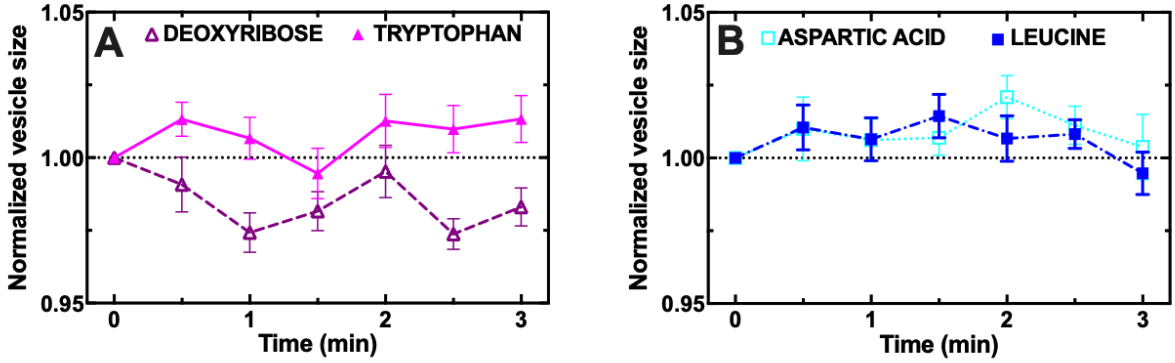

Figure S3. Metabolite permeation does not significantly affect vesicle size. Temporal dependence of the average vesicle size during the delivery of 1 mM deoxyribose (open triangles) or tryptophan (filled triangles) to **a)** archaeal 4ME diether G1PC vesicles, and **b)** leucine (filled squares) or aspartic acid (open squares) to bacterial diester G3PE-PG-CA vesicles. Mean (symbols) and standard deviation (error bars) were calculated by firstly normalising all values of each vesicle size to the size at t=0 and then averaging over the values measured on N=15 vesicles for each metabolite and membrane mimic. Corresponding permeability data for each metabolite and membrane mimic are presented in Figure 2. No significant change in vesicle size was measured during the delivery of deoxyribose or tryptophan to archaeal 4ME diether G1PC vesicles (p-value=0.27 and 0.36, respectively) or during the delivery of aspartic acid or leucine to bacterial diester G3PE-PG-CA vesicles (p-value=0.47 and 0.61, respectively). Moreover, no significant change in vesicle size or shape

was measured during the delivery of any of the metabolites in Figures 2. The lipids used for creating archaeal 4ME diether G1PC vesicles and bacterial diester G3PE-PG-CA vesicles are lipids 1 and 2, respectively, in Table S1.

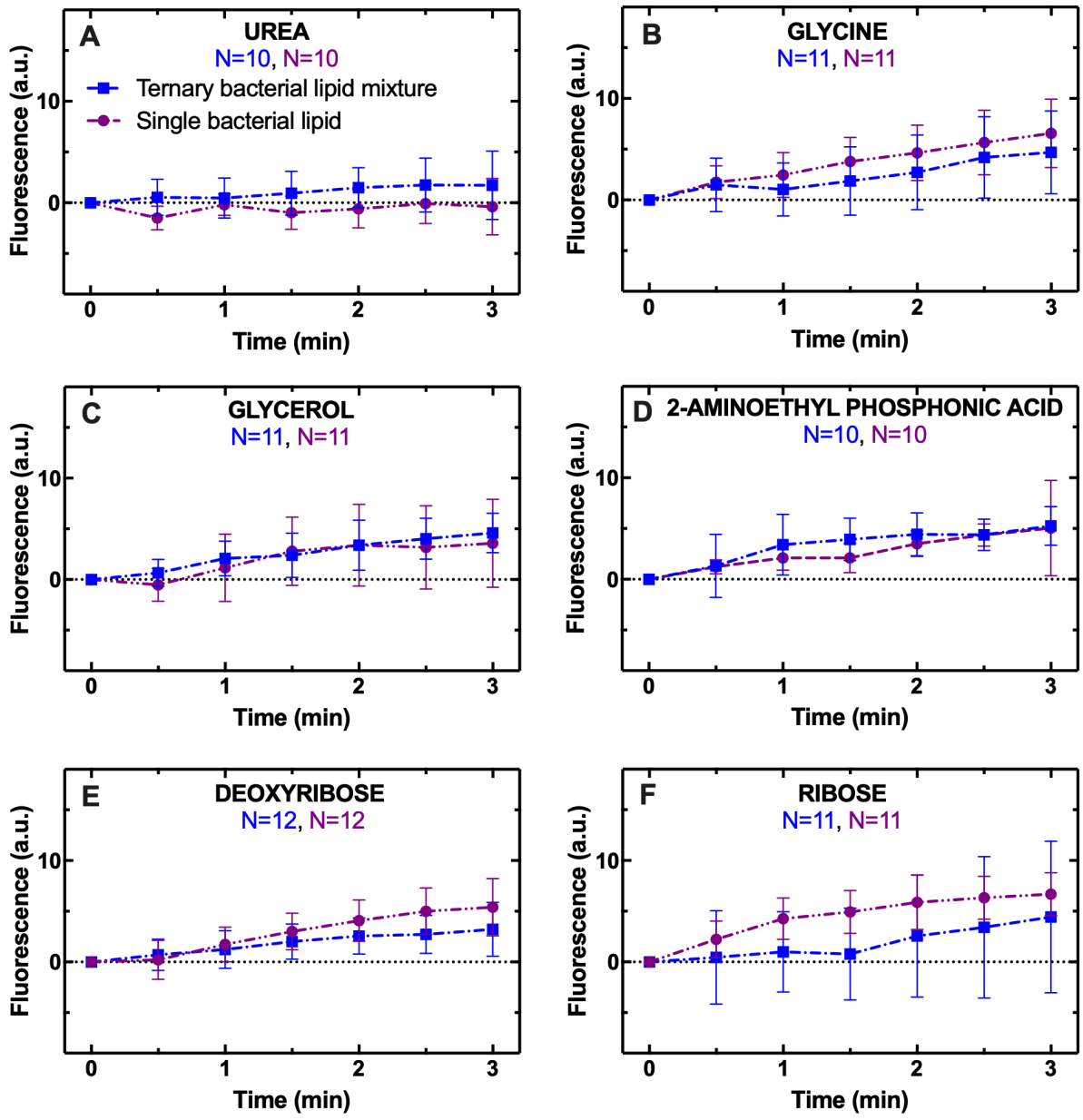

Figure S4. Mono- and ternary-lipid mixtures display similar permeability traits. Temporal dependence of average CF fluorescence in bacterial vesicles made of one lipid (purple circles) or a ternary lipid mixture (blue squares) during the exposure to 1 mM **a)** urea, **b)** glycine, **c)** glycerol, **d)** 2-aminoethyl phosphonic acid, **e)** deoxyribose or **f)** ribose delivered to the vesicles at t=0. Mean (symbols) and standard deviation (error bars) were calculated from at least 10 single-vesicle measurements across 3 independent experiments. N is the number of single vesicles investigated for each metabolite and each type of bacterial vesicle (blue and purple for ternary and single lipid vesicle, respectively). N varies across different metabolite-experiments investigated due to technical constraints (see Methods). However, care has been taken to obtain the same N for each metabolite-experiment across the two different type of lipid vesicles to ensure reliable statistical comparisons. Such comparisons have been carried out via two-tailed Mann-Whitney tests between the distributions of CF

fluorescence values at t=3 min for the mono- and ternary-lipid mixture. The lipids used for creating the bacterial membrane mimics with ternary and single-lipid mixtures are lipids 2 and 6, respectively, in Table S1.

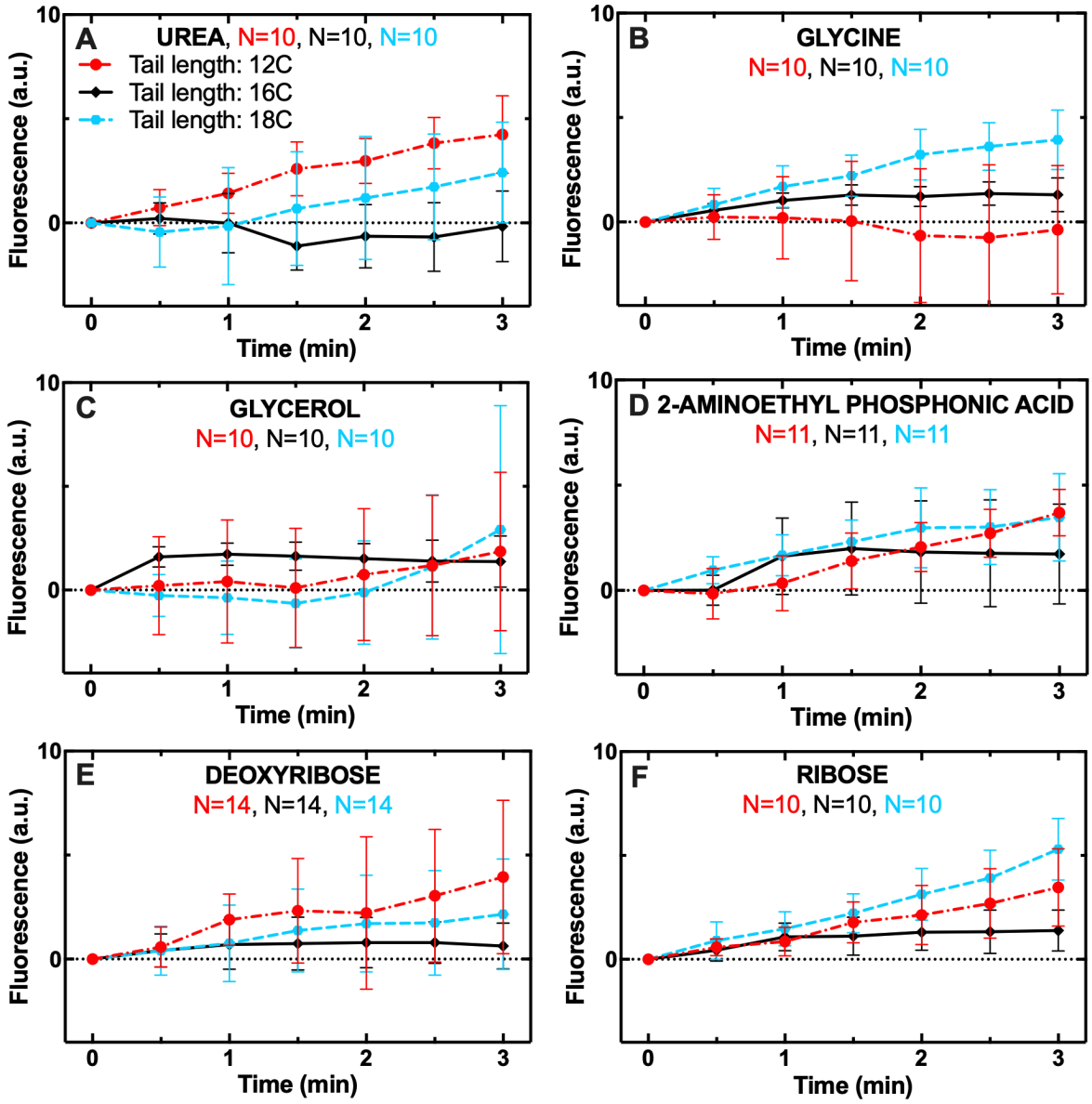

Figure S5. Lipid chain length does not have a significant impact on the permeability to core metabolites. Temporal dependence of average CF fluorescence in lipids with tail length of 12 (red circles), 16 (black diamonds) or 18 carbons (blue hexagons) during the exposure to 1 mM **a)** urea, **b)** glycine, **c)** glycerol, **d)** 2-aminoethyl phosphonic acid, **e)** deoxyribose or **f)** ribose delivered to the vesicles at t=0. Mean (symbols) and standard deviation (error bars) were calculated from at least 10 single-vesicle measurements (solid lines) across 3 independent experiments. N is the number of single vesicles investigated for each metabolite and each lipid length. N varies across different metabolite-experiments investigated due to technical constraints (see Methods). However, care has been taken to obtain the same N for each metabolite-experiment across the three different lipid lengths to ensure reliable statistical comparisons. Such comparisons were carried out by evaluating the Pearson correlation coefficient between the average fluorescence value at t=3 min and the tail length. The measured coefficients were -0.58, 0.95, 0.52, -0.10, -0.69 and 0.30 for urea, glycine, glycerol, 2-aminoethyl phosphonic acid, deoxyribose and ribose and not statistically significant for any of these

metabolites. We could not investigate the permeability of vesicles with chain length of 14 carbons (lipid 11 in Table S1) because the transition temperature of these lipids (i.e. 24 °C) is very close to room temperature and vesicles easily burst during our permeability assays. Finally, we could not form vesicles using lipids with a chain length of 6 carbons (lipid 10 in Table S1) despite attempting different electroformation protocols (Table S4). The lipids used for creating vesicles with tail length of 12, 16 and 18 carbons are lipids 8, 4 and 9, respectively, in Table S1.

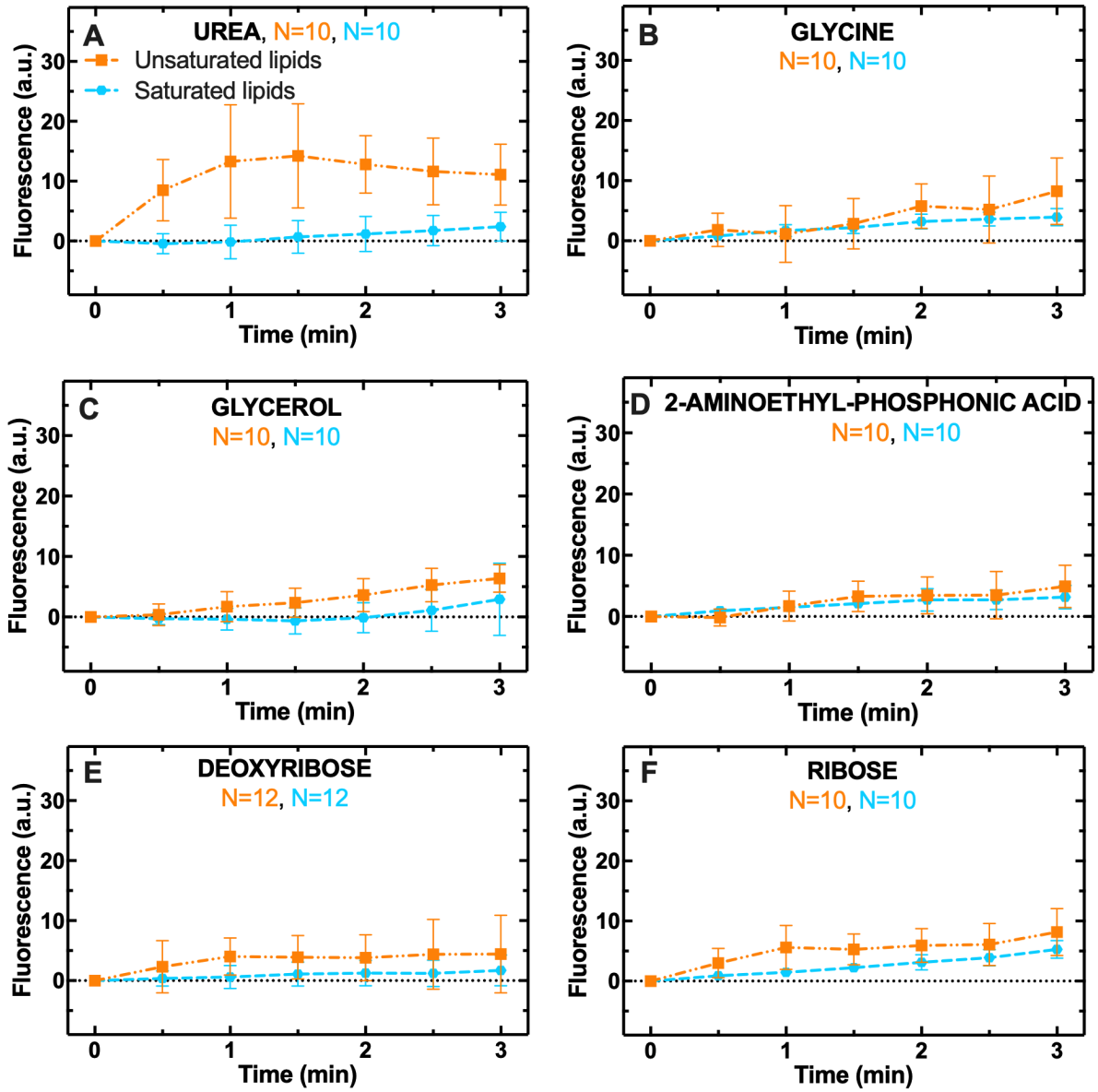

Figure S6. Unsaturated lipids favour permeability to urea and glycine. Temporal dependence of CF fluorescence in the presence (orange squares) or absence of double bonds along the lipid chain (blue circles) during the exposure to 1 mM **a)** urea, **b)** glycine, **c)** glycerol, **d)** 2-aminoethyl phosphonic acid, **e)** deoxyribose or **f)** ribose delivered to the vesicles at t=0. Mean (symbols) and standard deviation (error bars) were calculated from at least 10 single-vesicle measurements (solid lines) across 3 independent experiments. N is the number of single vesicles investigated for each metabolite and lipid type. N varies across different metabolite-experiments investigated due to technical constraints (see Methods). However, care has been taken to obtain the same N for each metabolite-experiment across the two different lipid types to ensure reliable statistical comparisons. Such comparisons have been carried out via two-tailed Mann-Whitney tests between the

distributions of CF fluorescence values at t=3 min for the single and double bonding lipid. The lipids used for creating the archaeal membrane mimics with and without saturation are lipids 9 and 12, respectively, in Table S1.

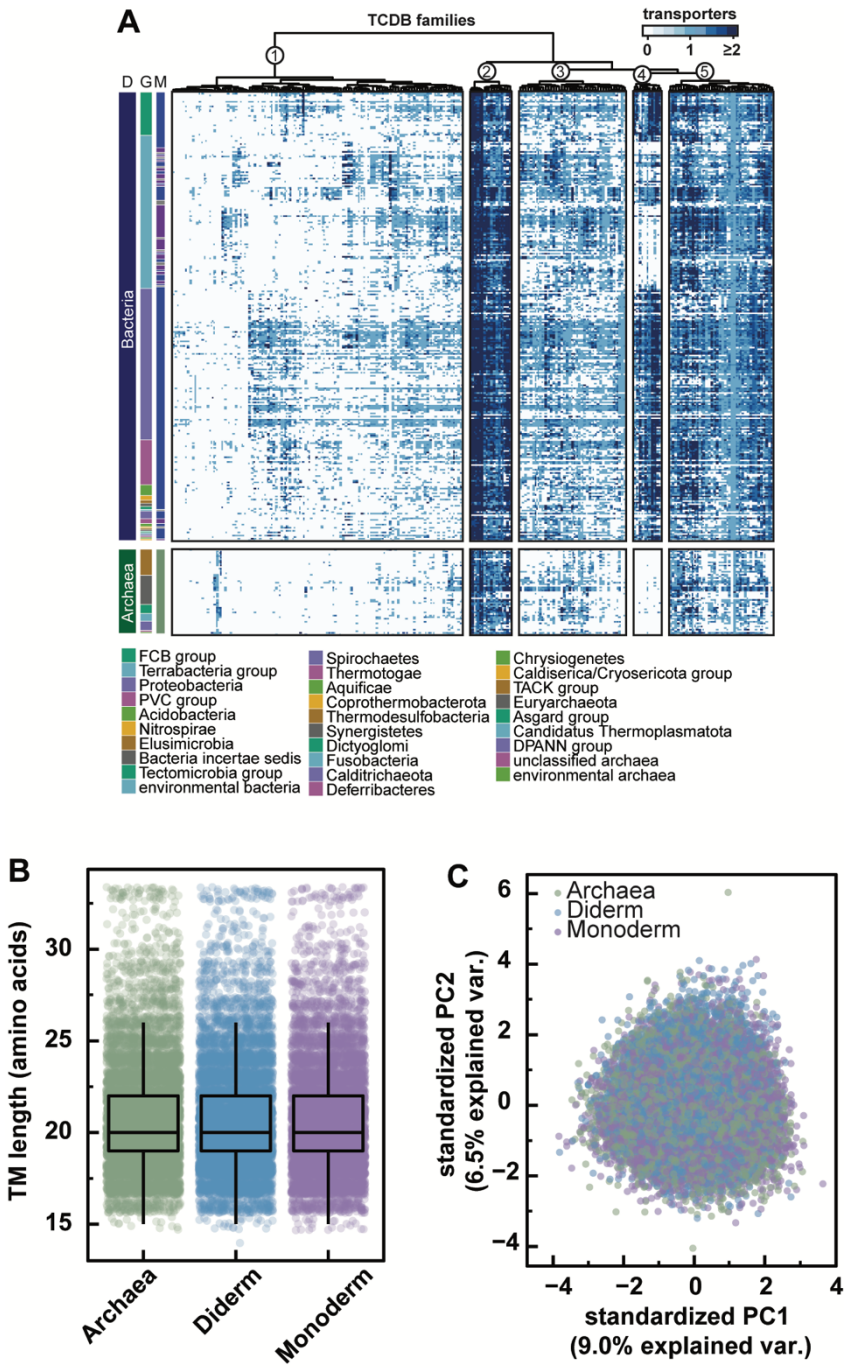

Figure S7. Archaeal and bacterial transmembrane domains are biochemically consistent. a) Heatmap showing transporter repertoires in Archaea and Bacteria, where each row and column represent a prokaryotic order and TCDB transporter family, respectively. Heat map values represent the median number of transporters across each prokaryotic order. The domain (D), group (G), and membrane morphology (M: where blue, purple, and grey, represent diderms, monoderms, and unknown membrane morphology, respectively) of each order is noted. TCDB families were grouped by hierarchical clustering based on transporter abundance using euclidean distances and the Ward.D2 clustering method. Taxonomy was based on NCBI Taxonomy classifications. **b)** Comparisons between the length of transmembrane domains in Archaea and bacterial

monoderms and diderms. Transmembrane domains were identified using Phobius. **c)** Principal component analyses based on the amino acid compositions of archaeal and bacterial transmembrane domains. In both analyses, archaeal and bacterial transmembrane domains were randomly subsampled to equivalent sample sizes (n=10,000).

Lipid	Lipid chemical structure/ IUPAC name	Mimic type/Avanti name	MW [g/mol]
1.	1,2-di-O-phytanyl-sn-glycero-1-phosphocholine 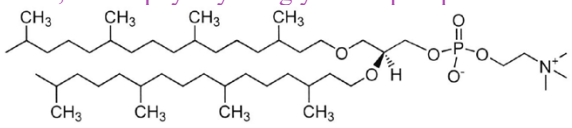	Archaeal 4ME 16:0 Diether G1PC	818
2.	1,2-dioleoyl-sn-glycero-3-phosphoethanolamine 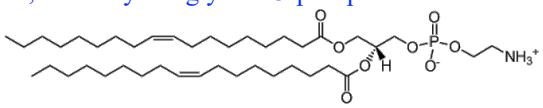	Bacterial Diester G3PE-PG-CA: 67% : 18:1 (Δ9-Cis) Diester G3PE	744
	1,2-dioleoyl-sn-glycero-3-phospho-(1'-rac-glycerol) 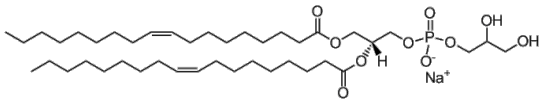	23.2% : 18:1 (Δ9-Cis) Diester G3PG	797
	1,3-*bis*(*sn*-3'-phosphatidyl)-*sn*-glycerol 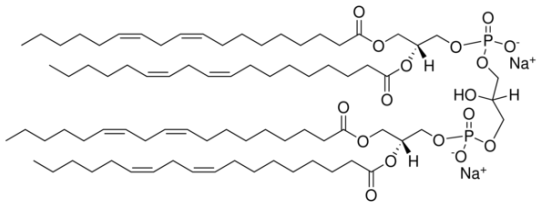	9.8% : Cardiolipin, sodium salt	1494
3.	1,2-di-O-phytanyl-sn-glycero-3-phosphocholine 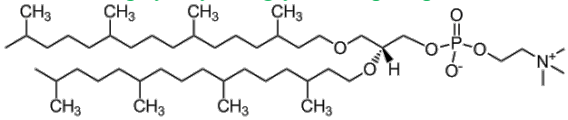	4ME 16:0 Diether G3PC	818
4.	1,2-di-O-hexadecyl-*sn*-glycero-3-phosphocholine 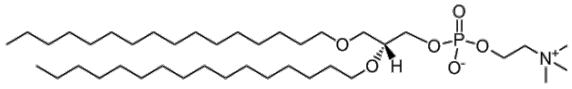	16:0 Diether G3PC	706
5.	1,2-diphytanoyl-sn-glycero-3-phosphocholine 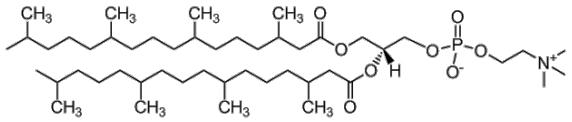	4ME 16:0 Diester G3PC	846
6.	1,2-dioleoyl-sn-glycero-3-phosphoethanolamine 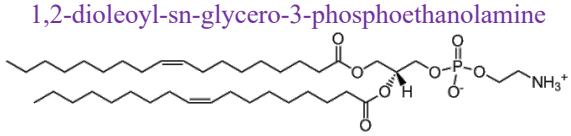	Bacterial 18:1 (Δ9-Cis) Diester G3PE	744
7.	1,2-di-O-phytanyl-sn-glycero-3phosphoethanolamine 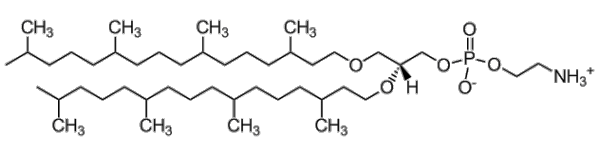	4ME 16:0 Diether G3PE	776

8.	1,2-di-O-dodecyl-sn-glycero-3-phosphocholine 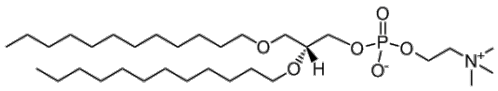	12:0 Diether G3PC	594
9.	1,2-di-O-octadecyl-sn-glycero-3-phosphocholine 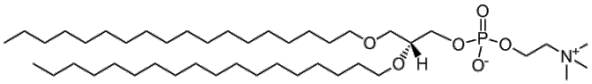	18:0 Diether G3PC	762
10.	1,2-di-O-hexyl-sn-glycero-3-phosphocholine 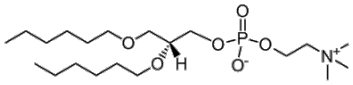	06:0 Diether G3PC	426
11.	1,2-di-O-tetradecyl-sn-glycero-3-phosphocholine 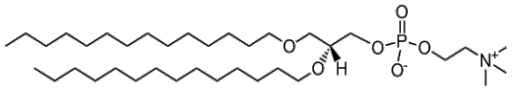	14:0 Diether G3PC	650
12.	1,2-di-O-(9Z-octadecenyl)-sn-glycero-3-phosphocholine 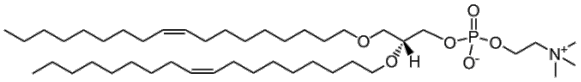	18:1 Diether G3PC	758

Table S1. Synthetic lipids employed to mimic archaeal and bacterial lipid membranes. List of lipids employed in this work, their chemical structure, their names according to the supplier (Avanti Polar Lipids within Merck) and their molecular weight. We could not produce vesicles using the lipids reported in grey due to technical limitations (see Methods).

Metabolite	Compound Class	MW [g/mol]	XLogP3	Charge	Rotatable bond counts	Fluorescence at t=3min Archaea	Fluorescence at t=3min Bacteria
Glycine	Amino acid	75	-3.2	0	1	13	1
Alanine	Amino acid	89	-3.0	0	1	10	-5
Leucine	Amino acid	131	-1.5	0	3	12	4
Aspartic Acid	Amino acid	133	-2.8	-1	3	5	-7
Glutamine	Amino acid	146	-3.1	0	4	8	2
Tryptophan	Amino acid	204	-1.1	0	3	11	2
Glyceraldehyde	Sugar	90	-1.6	0	2	11	1
Dihydroxyacetone	Sugar	90	-1.4	0	2	9	7
Deoxyribose	Sugar	134	-2.3	0	4	13	2
Ribose	Sugar	150	-2.5	0	0	15	7
Arabinose	Sugar	150	-2.5	0	0	11	6
Glycerol	Sugar alcohol	92	-1.8	0	2	10	5
Cytosine	Nucleobase	111	-1.7	0	0	10	6

Uracil	Nucleobase	112	-1.1	0	0	19	3
Adenine	Nucleobase	135	-0.1	0	0	10	5
Guanine	Nucleobase	151	-1.1	0	0	13	3
Urea	Amide	60	-1.4	0	0	19	3
(2-Aminoethyl) phosphonic acid	Phosphonate	125	-4.8	0	2	8	5
Adenosine monophosphate	Nucleotide	347	-3.5	0	4	NA	NA

Table S2. Physico-chemical and permeability properties of all metabolites investigated. List of metabolites investigated in this work, the class they belong to, their molecular weight (MW), hydrophobicity (decreasing with XLogP3), their charge, the number of their rotatable bonds, the measured average fluorescence of the archaeal or bacterial lipid membrane mimic after 3 minutes exposure to each metabolite.

Lipid	Frequency [Hz]	Amplitude [V]	Temperature [°C]	Time-rise [min]	Time-main [min]	Time-fall [min]	Outcome
1.	5	3	37	5	120	5	✓
2.	10	1.6	37	5	160	5	✓
3.	5	3	37	5	120	5	✓
4.	5	3	37	5	120	5	✓
5.	5	3	65	5	120	5	✓
6.	10	1.6	37	5	160	5	✓
7.	5	3	37	5	120	5	X
7.	5	3	65	5	120	5	X
7.	500	5.3	65	5	120	5	X
8.	500	5.3	65	5	120	5	✓
9.	500	5.3	65	5	120	5	✓
10.	5	3	37	5	120	5	X
10.	5	3	65	5	120	5	X
11.	5	3	65	5	120	5	X
12.	500	5.3	65	5	120	5	✓

Table S3. Protocols to obtain vesicles using synthetic lipids. Parameters for the protocols employed in this work. The protocols reported in grey yielded a negative outcome (see Methods).

Supplementary file 1. Statistical comparisons between permeabilities of two different lipid vesicle types. Summary of significance and p values estimated using two-tailed Mann-Whitney tests between distributions of CF fluorescence after 3 min of delivery of glycine, alanine, leucine, aspartic acid, glutamine, tryptophan, glyceraldehyde, dihydroxyacetone, glycerol, deoxyribose, ribose, arabinose, urea, cytosine, uracil, phosphonate, adenine or guanine to individual vesicles made of archaeal 4ME diether G1PC or bacterial diester G3PE-PG-CA lipids.

Supplementary file 2. Statistical comparisons between permeabilities of more than two different lipid vesicle types. Mean rank difference, summary of significance and p-value estimated using the Kruskal-Wallis one-way analysis of variance test between distributions of CF fluorescence after 3 min of delivery of urea, glycine, ribose, deoxyribose, glycerol and phosphonate to individual vesicles made of archaeal 4ME diether

G1PC, bacterial diester G3PE-PG-CA, 4ME diether G3PC, 16:0 Diether G3PC, or 4ME 16:0 Diester G3PC lipids.

Supplementary file 3. Identification of putative archaeal transporter families. Family: protein family identifier. Sequences: the number of archaeal proteins within a given protein family. Crossover: the percentage of proteins within a given family that were identified by TCDB HMM searches. TM domains: the median number of transmembrane domains per protein across sequences within a protein family. Archaeal_example_seq: a single UniProt accession number of an archaeal protein assigned to a given protein family. Archaeal_taxa: the number of archaeal species encoding proteins assigned to a given family. Bacterial_taxa: the number of bacterial species that contain homologs of a given archaeal protein family based on BLAST comparisons. Putative_transporter: a classification of whether or not a given protein family likely constitutes a transporter based on TCDB overlap and the presence of transporter-associated PFAM domains. Transporter_PFAMs: all PFAM domains assigned to a protein family that were assigned a transporter-associated domain. TopAnnotation: the majority-rule annotation for a given protein family assigned using eggNOG mapper. %withAnnot: the percentage of sequences that were assigned the majority-rule annotation. TotalAnnotSeqs: the number of sequences within the protein family that were successfully annotated. TotalSeqs: the total number of sequences analysed.